Spatial transcriptomics of glioblastoma defines biologically and clinically significant reprogramming patterns across unique spatial microenvironments

Visweswaran Ravikumar[1,+,*], Avery Maddox[1,+], Reva Kulkarni[1,+], Arvind Rao[1,3,4,*], and Wajd N Al-Holou[2,*]

[1]Department of Bioinformatics and Computational Medicine, University of Michigan, Ann Arbor, MI, 48109, USA
[2]Department of Neurosurgery, University of Michigan, Ann Arbor, MI, 48109, USA
[3]Department of Biostatistics, University of Michigan, Ann Arbor, MI, 48109, USA
[4]Department of Radiation Oncology, University of Michigan, Ann Arbor, MI, 48109, USA
[*]vravik@umich.edu, ukarvind@umich.edu, wna@umich.edu
[+]these authors contributed equally to this work

ABSTRACT

Glioblastoma (GBM) is the most common and lethal primary malignant tumor of the central nervous system. Advances in therapy are hindered by the complex intratumoral heterogeneity of GBM, where distinct malignant and non-malignant cellular states and interactions exist in spatially defined niches of the tumor microenvironment (TME), shaping both tumor behavior and treatment response. In this work, we define GBM biological reprogramming, TME recomposition, and cell-cell interactions in relation to spatially well defined Ivy Glioblastoma Atlas Project regions. Further, we apply a novel spatially informed approach to integrate biological reprogramming, as identified through gene co-expression network modules, with specific changes in cell-cell communications. Our results validate prior findings and offer novel insights into the spatial patterning of transcription factor regulation, cellular interactions, and biological pathway activity, in addition to informing rational combination therapies targeting spatial niche specific vulnerabilities. In addition, our work contributes a novel Visium spatial transcriptomics dataset of 14 samples for use by the GBM research community.

Introduction

Glioblastoma (GBM) is the most common primary malignant tumor of the central nervous system (CNS), accounting for 48.6% of malignant CNS tumors [1]. In addition, it is one of the most lethal malignancies, with a median survival of only 15 months and a 5-year survival of only 7% [1, 2]. Despite significant advances in the understanding of GBM and the identification of many novel therapeutic targets, the prognosis remains poor and the standard of care has not changed significantly in the last 15 years [2]. A major obstacle to advancing GBM therapy, indicated by its historical designation "Glioblastoma Multiforme", is its extreme intratumoral heterogeneity [3]. Throughout and around the GBM tumor, distinct malignant and non-malignant cellular states, behaviors, and interactions exist in spatially defined microenvironmental niches that aid in the development of treatment resistance and tumor recurrence [3]. Elucidating the spatial context and patterning of this heterogeneity is therefore critical to advancing our understanding and treatment of GBM.

Significant work has been performed to help explain the spatial patterning of GBM heterogeneity and has provided important insights for improving treatment. In early work on this front, the Ivy Glioblastoma Atlas Project (Ivy GAP) integrated in-situ hybridization, laser microdissected RNA sequencing, and high-resolution imaging to define and map distinct GBM tumor regions including: leading edge (LE), microvascular proliferation (MVP), cellular tumor (CT) and pseudopalisading around necrosis (PAN) [4, 5]. More recently, spatial transcriptomics (ST) analysis has revealed important GBM patterning in relation to these regions including: immune tumor microenvironment (TME) changes in relation to perivascular and perinecrotic regions [6], distinct glioma stem cell (GSC) signatures in relation to perinecrotic and peritumoral regions [7], and distinct glioma cell states in neuron rich regions [8]. Additionally, a significant role for hypoxic stress gradients, which largely drives the patterning of Ivy GAP regions, has also been closely tied to the spatial patterning of GBM cell states, molecular behaviors, and treatment resistance [9, 10]. Further studies have also helped spatially define the intercellular interactions in the GBM TME and relate these interactions in their spatial niche to tumor progression and treatment resistance [11].

In this work, we advance the spatial understanding of GBM heterogeneity in important ways. We present a novel high-quality Visium ST dataset of 14 slides from 7 GBM patients, and perform integrative analysis of our cohort with the Freiburg

[12] and Broad [9] studies. Together, our sample size includes 44 tumor slides and 128,176 spots after QC filters. Thus our work presents findings from one of the largest GBM ST datasets analyzed to date, significantly enhancing confidence both where our study recapitulates prior findings as well as where we present novel results. Using marker genes provided in the Ivy GAP study, we annotated every spot into distinct niches. Differential expression analysis validates many previously described results about distinct activation of biological pathways and hallmark features across tumor niches. Using state-of-the-art deconvolution algorithms, we modeled cellular communities across the tumor niches and extract tumor-specific expression profiles per spot. We further used this data to model continuous rewiring of tumor expression profiles and transcription factor (TF) modules along spatial gradients. We identify specific TFs that are active along specific niche interfaces, suggesting localized vulnerabilities in the tumor cells.

To elucidate spatially driven changes in GBM molecular behavior at the pathway level, we employed high dimension weighted gene co-expression network analysis (hdWGCNA) [13] on our ST dataset. Through gene co-expression network (GCN) analysis we identify many distinct pathways upregulated in association with specific Ivy GAP regions including: NOTCH signaling pathways in CT, inflammatory pathways in MVP, hypoxic stress response in PAN, and neuron projection development in LE. In addition, we identify potential drivers and therapeutic targets of these pathways and place dozens of previously identified GBM-related genes into a spatial functional context.

To further the understanding of spatially patterned cell-cell interactions in GBM, we integrate our ST data with a comprehensive GBM single-cell (SC) atlas [14] to map TME niche-specific ligand-receptor (LR) interactions. Specifically, we intersect LR interactions in the SC data with spatially co-expressed LR interactions in the ST data. We further explore the downstream consequences of these interactions, linking cell communication events to tumor phenotypes elucidated by the ST GCN. Our results reveal key microenvironment-driven mechanisms of cellular reprogramming and potential intervention strategies. Notably, we identify tumor cell state differentiation modulated by EGFR signaling in CT, dual pro-tumor (angiogenesis) and anti-tumorigenic mechanisms driven by integrin and immune signaling in MVP, immune evasion and cell plasticity driven by cytokine and FN1/SPP1-CD44 signaling in PAN, and invasion driven by neuronal guidance via ephrin signaling in LE.

By using a large cohort of Visium ST slides and cutting-edge analytical tools and techniques, we present a comprehensive overview of tumor biology across the diverse spatial niches in GBM. Our analysis, outlined in Figure 1, reveals extensive tumor plasticity and variability of regulatory programs across spatial micro-environments, and hints to why targeted therapies against single molecular markers are likely to be ineffective. Using our integrative analyses, we are able to highlight specific localized vulnerabilities of the disease, which informs combination therapy development targeting these pathways and could lead to better therapeutic outcomes for patients.

Figure 1. Graphical summary of study. Spatial RNA-Seq data from resected glioblastoma tumor was collected across multiple cohorts, annotated for anatomical niches using Ivy GAP markers, and then deconvolved to obtain cell type proportions and tumor specific expression. Diverse analysis were applied to this data including: differential expression analysis at the gene and pathway level; transcription factor network analysis; ligand-receptor analysis, incorporating additional single cell RNA-Seq data to enhance performance; and finally gene coexpression network analysis. This integrative analysis produced niche specific biological insights including distinct ligand receptor interaction driven pathway activity.

Results

GBM anatomical niches are associated with distinct biological programs and microenvironment compositions

We performed Visium spatial profiling of 14 tumor slides from seven GBM patients. Spot level niche annotation was performed by scoring for the Ivy-GAP maker genes from [4] using the UCell algorithm [15]. Figure 2A,B shows a representative tumor tissue slide and corresponding marker-based region annotations. The anatomical composition across our profiled ST slides vary widely (S1A Fig) with the CT and PAN regions being the most represented niches in our dataset (S1B Fig). Only 3151 spots that were assigned to LE niche, predominantly coming from a single tumor slide (8379-B). Since this might highly skew our results because of inter-patient heterogeneity, we pooled our data with publicly available Visium ST slides from two recent studies that we label as the Freiburg [12] and Broad [9] cohorts. Our final dataset includes 17 slides from the Freiburg cohort, 13 slides from the Broad cohort and 14 of our own slides, and a total of 128,176 spots. The relative Ivy niche composition of each cohort is shown in Figure S1C. The Freiburg cohort captured more LE during data acquisition and provides a good representation of this niche. The annotation breakdown in our pooled dataset is (65742, 8992, 33266, 20176) spots in the (CT, MVP, PAN, LE) niches respectively. Having ensured we have sufficient representation of these niches, we proceed to characterize the changes in gene expression programs and TME compositions between them.

Figure 2. Molecular features of tumor microenvironments in GBM. (A) Representative histology slide of ST sample. (B) Ivy GAP marker-based annotation of anatomical niches. (C) Enrichment analysis of differential genes across niches. (D) Top-5 differential Hallmark pathways. (E) Scaled abundance of cell types in tumor niches. (F) Localization of Neftel tumor states to distinct spatial niches in slide 1512-A. (G) 2D PCA embedding captures continuous spatial gradients across multiple slides. (H) Localization of Neftel tumor state enrichment to specific domains in embedding space.

Differential expression analysis across tumor niches identified 2,642 significant genes, with the infiltrative edge exhibiting the most distinct transcriptional profile. Gene ontology (GO) term enrichment analysis of these genes revealed biologically coherent patterns (Fig 2C): vasculature development and angiogenesis pathways were enriched in MVP regions, while hypoxia-response signatures predominated in PAN areas. Across the tumor bulk, we observed significant enrichment for extracellular matrix (ECM) activity, consistent with reports that GBM cells actively remodel the ECM to support survival and proliferation [16]. CT regions showed upregulation of neuronal activity, glial cell differentiation, and Notch signaling, the latter of which is known to maintain the stemness of neuronal precursor cells and inhibit terminal differentiation [17, 18]. Finally, the tumor LE was uniquely enriched for neuronal signaling and synaptic activity, likely reflecting the integration of glioma cells with surrounding neural networks [19].

Comparison of enrichment scores for Cancer Hallmark signatures also showed extensive variability across spatial domains. Figure 2D shows scaled pseudo-bulk activity of top-5 Hallmark pathways in each niche. The niche-specific roles of several of these pathways have been previously characterized in literature. For example, protein secretion through non-canonical secretion pathways is a known hallmark of the GBM core [20]. Secretion of ECM proteins by tumor cells has been shown to significantly alter the tumor microenvironment to enhance tumor cell motility and invasiveness [21]. Furthermore, secretion of soluble proteins such as CD109 is known to facilitate crosstalk with invasive cells on the tumor margins to promote disease progression [22]. The MVP and PAN regions share enrichment of the complement signaling and coagulation pathways, which are associated with a variety of functions including vascular remodeling, modulation of immune activity and supporting tumor cell survival [23, 24, 25]. We also observe strong EMT activity in the MVP niche, as shown in Figure S1D.

Cells in the LE have significant enrichment for mitotic spindle activity. This hallmark is closely linked to both tumor proliferation and invasiveness, and it's known that cytoskeletal remodeling aids tumor cell migration and invasion in this niche [26]. We also observe distinctly high UV response activity in the LE and PAN regions, suggesting robust DNA damage response activities [27]. Interestingly, it's been shown that while the PAN niche has high capacity for sensing DNA damage, it is associated with increased genomic instability due to downregulation of DNA-damage repair mediators [28]. Consequently, the hypoxic regions have been shown to accumulate chromosomal alterations and contribute to subclonal evolution of the tumor [12]. In contrast, tumor in the LE does have robust DNA repair activity that makes these infiltrative cells resistant to chemo- and radiation therapy and leads to tumor recurrence [29]. Further, this niche also shows enrichment for adipogenesis, fatty acid oxiation and heme metabolism processes. These metabolic adaptations have been shown to be differentially enriched in tumor margins relative to tumor core [30], and facilitate adaptability of cancer cells to distinct nutrient environments, supporting their survival and invasive phenotypes [31, 32]. Our results robustly confirm the activity of several previously described niche-specific biological programs in GBM, supported by analysis of a large, multi-patient ST dataset.

To resolve TME cellular architecture, we performed reference-based deconvolution of 44 spatial slides using a harmonized GBM SC atlas [14] and the InstaPrism algorithm [33]. The inferred cell type abundance matrix was modeled as compositional data, and used to construct a sparse cell-interaction graph shown in Figure S1E. Consistent with the concept of a layered organization of the GBM TME [9], we see that cell-types have limited positive interactions with other TME components, alongside numerous negative interactions indicating localized distribution in distinct spatial regions. We observe preferential interactions of the different tumor cell states with specific immune and neuronal cell types. We see strong interactions between AC/OPC-like tumor states, Endothelial and Mural cells, TAM-MG and TAM-BDMs, MES-like and Mural cells, neurons and NPC-like cells.

In order to see what regions these interactions are localized to, we plotted the scaled mean cell type abundances by the spot annotations in Figure 2E. As with gene expression programs, we see a clear transition in the TME composition between tumor niches. We observe increased abundance of endothelial and immune cells in the MVP [34]; prevalence of radial glia, plasma cell, neutrophil and monocyte infiltration in PAN regions [35]; and higher prevalence of microglia in the CT and the LE spots [36]. Bone-marrow derived macrohpages (BDMs) are most prevalent in the MVP, where they have been shown to interact with endothelial cells to promote angiogenesis [37]. Glial and neuronal cells are distinctly prevalent in the LE. We also note strong localization of different Neftel tumor states to specific niches, with the NPC-like cells localized to the LE; AC- and OPC-like cells most prevalent in the perivascular niches; and MES-like tumors most abundant in the hypoxic areas. We visualize the patterns of distinct tumor-state localization to particular niches in our representative slide 1512-A in Figure 2F. Our observation is consistent with known localization patterns of these tumor states to specific ME niches, and indicates the significant power of

spatial context in the TME to shape cellular expression programs [38].

We next sought to quantitatively characterize continuous transitions in tumor expression programs as a function of their spatial microenvironment. Our objective was to model how gene expression profiles, cellular compositions, and intercellular signaling interactions shift along spatial gradients, with a particular focus on identifying TFs that orchestrate these cell state transitions across the tumor continuum. To facilitate this analysis jointly across all 44 ST slides, we generate a supervised PC embedding using batch-corrected expression for the Ivy GAP marker genes in each spot (see Methods for details). This low-dimensional embedding succinctly recapitulates the major axes of transcriptional variation between tumor niches, yielding a unified manifold for downstream spatial analyses (Fig 2G). As depicted in Figure S1F, this embedding faithfully represents continuous gradients in Ivy GAP niche-specific enrichment scores, with spatially proximal spots in the original tissue architecture mapping to neighboring coordinates in the PCA space. Figure 2H shows localization of enrichment scores for the Neftel state [39] marker genes in the PC embedding, capturing fine-scale distinctions in relative localization patterns of the MES1/MES2 and NPC1/NPC2 tumor cell states. The MES2 signature was specifically enriched in extreme PAN regions, consistent with its established association with hypoxia-responsive programs in GBM [39, 40]. Within the NPC-like compartment, the NPC2 program localized to the tumor leading edge, identifying highly proliferative, progenitor-like populations in the invasive margin, while the NPC1 signature was prominent in the cellular tumor core, marking a more differentiated, less proliferative state [41].

Spatial gradients drive continuous molecular reprogramming in tumor cells

Given the limited resolution of Visium ST data and the potential confounding effects of microenvironmental heterogeneity on spot-level expression profiles, we employed the BayesPrism algorithm [42] to deconvolve cell type composition and extract tumor cell–specific expression data for each spot. BayesPrism utilizes a Bayesian framework to jointly infer the posterior distributions of cell type proportions and cell type–specific gene expression, leveraging SC RNA-seq references to improve robustness against both technical and biological variation [42]. The algorithm has been rigorously benchmarked [43, 44] for its ability to accurately recover malignant cell expression profiles in ST data and has been successfully applied to extract tumor-specific expression in published studies of GBM samples [42]. For additional quality control, we excluded spots with fewer than 200 tumor unique molecular identifiers in the tumor expression matrix, thereby filtering out regions with insufficient tumor cell content. The resulting tumor-specific expression matrix was normalized and used to investigate spatial variation in gene expression across anatomical niches.

To address potential confounding from variable tumor cell composition in our initial differential expression analyses, we performed a tumor cell–specific differential expression analysis to robustly identify genes and TFs exhibiting significant changes between spatially defined tumor microenvironments. Recognizing that tumor spots exist along a spatial continuum, we leveraged the relative enrichment scores derived from our integrated embedding to select the top 3,000 scoring spots for each niche. Differential expression analysis identified a total of 3,700 genes, underscoring the extensive transcriptional rewiring that occurs as tumor cells adapt to distinct microenvironmental contexts. Functional enrichment analysis of these genes (Fig 3A) revealed region-specific biological programs: the CT region was enriched for pathways related to DNA replication, cell cycle regulation, differentiation, and cell motility; the MVP region showed upregulation of ECM reorganization processes; PAN regions were characterized by enrichment of hypoxia response, apoptotic signaling, and wound healing pathways. These findings are consistent with prior reports that the mesenchymal (MES) state in hypoxic GBM regions recapitulates an injury-response inflammatory signature [45]. In the LE, invasive tumor cells exhibited upregulation of genes involved in synaptic communication and transmembrane potential, indicating a functional integration with the surrounding neuronal microenvironment [46]. In parallel, we identified 343 TFs with significantly altered expression across spatial niches, with 246 showing highest expression in the CT region, highlighting the remarkable transcriptional diversity and regulatory complexity within this compartment. Figure 3B presents the top five differentially expressed TFs for each niche, illustrating the distinct regulatory landscapes that underpin spatial heterogeneity in GBM.

Figure 3. Spatially-driven adaptations of tumor cells in GBM. (A) GO Enrichment analysis of tumor-specific differential expression test between GBM niches. (B) Scaled expression of Top-5 differentially expressed transcription factors in each niche. (C) Hotspot analysis identifies 9 distinct TF modules with spatially localized activity across all slides. Localized activity scores of representative TF modules in PC space. (D) Correlation plot between different TF modules shows spatial segregation of their activity. (E) Enrichment analysis of differential genes in spots enriched for specific TF module activity. (F) Comparative analysis of Module-9 enriched spots with CT and LE modules identifies biological processes specifically active in the interface.

We next sought to identify the regulatory factors driving transitions in expression programs along niche interfaces. To this end, we applied the Hotspot algorithm [47], a graph-based method for detecting genes and gene modules with significant localized expression patterns in SC and ST data. Hotspot operates by defining a cell–cell similarity metric—such as spatial proximity or position in a reduced-dimensional embedding—and identifies genes whose expression is autocorrelated among

neighboring cells or spots. By clustering genes with similar expression patterns, Hotspot delineates modules that likely represent coordinated regulatory programs active in specific tissue contexts. We constructed a neighborhood graph using our unified PC embedding, and systematically assessed the expression of all known human TFs [48] in this space. Hotspot identified 184 TFs with significant spatial autocorrelation in expression ($FDR < 0.05$), which were split into nine modules of covarying factors (Fig 3C) (see Methods for details). TF modules showed niche-specific activation: for example, Module 2 was distinctly enriched in the perinecrotic (PAN) region, while Module 5 was active at the leading edge (LE) (Fig 3C).

Visualization of module activity in both the PC embedding and spatial coordinates of slide 1512-A (S2A Fig) revealed that the majority of TF modules (Modules 1, 3, 4, and 7) are concentrated around perivascular niches, indicating substantial and distinct regulatory processes in these regions. Module 6 also exhibited unique activity within vascular areas, while smaller modules (Modules 8 and 9) were predominantly active along the CT-to-hypoxic and CT-to-LE transition zones, respectively. Correlation analysis of module activity across all spots (Fig 3D) recapitulated the spatial segregation of regulatory programs. Modules 8 and 9 were weakly correlated with the CT modules and anticorrelated with each other, highlighting their distinct roles along different spatial interfaces. These results suggest that specific TF modules orchestrate localized gene expression programs as tumor cells adapt to their microenvironment [40, 49].

To assess whether TF modules identified in our analysis are associated with specific biological programs along spatial interfaces, we selected the top 1,000 highest-scoring spots for each module and compared their gene expression profiles. Although many TF modules showed peak activity in the peri-vascular region, their enrichment was spatially distinct, resulting in minimal overlap among the top spots for each module. This spatial segregation suggests a fine-grained organization of biological processes, particularly within perivascular regions, consistent with recent studies demonstrating niche-specific regulatory programs and the compartmentalization of tumor-cell phenotypes [6, 8, 12].

GO term enrichment analysis (Fig 3E) revealed that each TF module is associated with a distinct set of biological processes. Modules 1, 3, and 4 are primarily linked to cell division and DNA replication, reflecting proliferative programs that are spatially confined within the tumor core and perivascular regions [8]. Module 6 is specifically enriched for cytoskeletal organization and cell motility, aligning with the known roles of perivascular niches in supporting tumor cell migration and invasion [50, 51]. Module 7 shows distinct enrichment for RNA splicing processes. Alternative splicing is emerging as a critical disease mechanism in GBM, generating transcript diversity that contributes to tumor heterogeneity and impacts neural developmental hierarchies [52, 53]. Co-localization of activity of these diverse TF modules around vascular structures underscores the multifaceted nature of perivascular tumor adaptation. The PAN-specific Module 2 is enriched for pathways related to adaptation to hypoxia and nutrient deprivation, as well as developmental processes indicative of GSC maintenance-findings that are consistent with the immunosuppressive and stem-like character of the perinecrotic niche [10, 54]. Module 5, active at the LE, is enriched for neuronal signal transduction, synaptic signaling, and mitochondrial ATP synthesis, suggesting that tumor cells at the invasive margin are both highly metabolically active and potentially integrating into neural circuits. Module 8, which is active at the CT–PAN interface (S2A Fig), is associated with diverse metabolic processes, reflecting metabolic reprogramming as tumor cells transition toward hypoxic environments. Module 9, localized to the CT–LE interface (S2A Fig), shows enrichment for neurodevelopmental processes, synapse organization, and axonogenesis, indicating that tumor cells in this region may be acquiring neuronal phenotypes as they prepare to invade the brain parenchyma.

While metabolic adaptations along the CT-PAN gradient are well-documented in GBM biology, Module-9 emerged as a novel and unexpected regulatory hub. This TF module, visualized in Figure S2B, encompasses SOX-family members (e.g., SOX2, SOX9), which are central to maintaining GSC self-renewal and pluripotency [55], alongside neurodevelopmental regulators such as FOXG1 and POU3F2-both implicated in promoting GSC stemness, invasive potential, and resistance to therapy [56, 57]. The module also includes hypoxia-responsive (HIF1A) and matrix-remodeling (YBX1) factors, which drive adaptive responses to microenvironmental stress and facilitate tumor cell migration [58]. The coordinated activity of these TFs at the CT-LE interface suggests a transcriptional program that primes GSCs for proliferative expansion and parenchymal invasion, potentially through metabolic rewiring and synaptic integration with neuronal networks [32].

To delineate biological mechanisms specific to this interface, we performed differential expression analysis specifically comparing gene expression along this gradient. We selected the top-1000 scoring spots for the CT and LE Ivy GAP markers, and 1000 spots with strongest Module-9 activity. This revealed 940 genes significantly upregulated in Module-9 spots, with pronounced enrichment for mRNA splicing/processing and neurodevelopmental pathways (Fig 3F). The alternative splicing machinery is overrepresented, aligning with the demonstrated role of this molecular mechanism in inducing neural stem-like states in GSCs and enhanced adaptability to microenvironmental challenges [53, 59]. These findings implicate post-transcriptional regulation as a critical driver of invasive phenotypes, suggesting targeting spliceosomal components as a potential strategy to contain tumor spread.

Figure S2C displays the mean activation scores of each TF module across all 44 ST slides. The relative activity of individual TF modules varies substantially between slides, reflecting the underlying heterogeneity in niche composition observed in Figure S1B. This variability is consistent with the highly localized and niche-specific activation of TF modules, many of which are

confined to distinct spatial interfaces that may only be present in a subset of samples. Our findings highlight the necessity of profiling a large and diverse cohort of tissue sections to capture the full spectrum of spatial regulatory heterogeneity in GBM. By leveraging a unified 2D embedding across all 44 slides, we are able to systematically analyze spatial trends in gene regulatory programs across TME niches, overcoming the limitations of single-sample analyses. This has allowed us to discover spatially restricted therapeutic vulnerabilities of the cancer cell in GBM. Motivated by these findings, we proceeded to apply network analysis to identify further pathways in a data-driven fashion and closely investigate their associations with distinct spatial niches as well as the central genes and cellular interactions driving their behavior.

AREG - EGFR and ECM - CD44 signaling promotes specific tumor state and glioma stem cell patterns in CT

The core tumor (CT) consists of the central tumor mass, defined by both undifferentiated glial cells and the start of tumor proliferation and specialization.

To identify and characterize Ivy GAP region driven pathway alterations, we applied hdWGCNA to our ST dataset of 44 slides, identifying 19 GCN modules which we labeled M1 to M19 (see Methods for details). Module eigengenes (MEs), the first principal component of a module's gene expression profile, provide a single continuous value capturing the activity level of a module. One-vs-all differential ME analysis revealed 11 upregulated modules in CT relative to the rest of the tumor sample, with the top 5 in order of decreasing log fold change (LFC) being: M14, M13, M16, M15 and M8 (Fig 4A). In addition, linear mixed effect modeling of ME values by IVY region assignment showed increases in M14, M13, M16, and M15 expression relative to LE, MVP, and PAN regions (Fig 4B). M8 is upregulated relative to MVP and PAN regions, but is not significantly upregulated relative to LE (Fig 4B).

Figure 4. CT specific pathway and LR analysis. (A) One-vs-all testing of MEs in CT relative to the rest of the tumor. Circles marked "x" where FDR > 0.05. (B) Coefficients from mixed effect modeling of ME against IVY region assignment, ME change shown in relation to CT level. "*" where FDR < 0.05. (C) Top pathway terms for 5 most upregulated modules in the CT. (D) Top drugs by significance of gene target enrichment for 5 most upregulated modules in CT. (E) CellChat communication scores for top LR pairs whose spatial co-expression is associated with CT. Note, as score is dependent on expression values, scoring is relative across cell type combinations and LR pairs. (F) T-values from lr-module regression specific to CT LR pairs. Modules shown are differentially expressed in CT. (G) Spatial plots of IVY region assignment and select LR coexpression and ME scores. (H) Network visualization of top 10 hub genes for the 5 most upregulated modules in CT.

Enrichment analysis of M8 highlights its primary roles in glial differentiation, myelination and related fatty acid metabolism (Fig 4C). Module hub genes, those genes most closely associated with their ME, offer more nuanced insights into drivers and regulators of module behavior. M8 hub gene CLDN11 (Fig 4H) has been shown to be specifically upregulated in GSC differentiation [60]. Hub genes PLP1 and CNP are markers for the Neftel OPC tumor state [39]. MOG and MOBP oligodendrocyte markers further indicate that the M8 pathway represents a distinct GSC differentiation pathway to an oligo-like state [61, 62]. This coincides with findings from Figures 2H and S1F, which show an overlap with the Neftel OPC tumor state and CT spots. Interestingly, M8 hub genes ERMN, MOBP, and PLP1 were previously identified in a study of 4 GCN hub genes whose upregulation was associated with a lower Karnofsky Performance Status score in older GBM patients [63]. In summary, M8 represents an OPC-like niche with evidenced links to functional status changes in GBM patients.

M14 is enriched for NOTCH signaling pathways, GSC program activation, and proneural subtype signature genes (Fig 4C). This CT upregulation of NOTCH signaling recapitulates findings from our differential expression analysis (Fig 2C). M14 hub genes (Fig 4H, S6 Table) including NOTCH1, HES6, SOX8, MARCKSL1, and OLIG2 implicate M14 in GSC proliferation and maintenance [64, 65, 66, 67, 68]. HES6, MARCKSL1, OLIG1 and BCAN further suggest M14 is closely related with the Neftel NPC1 tumor state [39]. Again, this coincides with findings from Figures 2H and S1F, which show an overlap with the Neftel NPC1 tumor state and CT spots. ECM related hub genes BCAN and CSPG5, along with hypoxia driven HES6 highlight particular environmental conditions associated with this M14 functionality [69, 70, 71]. Interestingly, PDE inhibition has shown promise for GBM therapy [72, 73] and M14 is enriched for targets of 3 closely related PDE3 inhibitors: Enoximone, Milrinone, and Amrinone (Fig 4D). Together these highlight a specific GSC promoting NPC1-like niche that may be targeted through PDE inhibition.

M15 is enriched for mitosis related pathways, including the G2-M checkpoint (Fig 4C). This mitotic upregulation further validates results from our TF modules showing increased DNA replication and cell division in the CT. Upregulation of M15 hub genes (Fig 4H) UHRF1, UBE2C, BIRC5, NUSAP1, TOP2A, RRM2, TYMS, PTTG1, and HMGB2 have all been independently identified in prior work for promoting proliferation, preventing apopoptosis or both in GBM [74, 75, 76, 77, 78, 79, 80, 81]. The one exception of the top 10 hub genes is TTYH3, which is related to volume regulation in the brain through anion and osmolyte efflux [82], and may be important here in managing tumor growth accommodating volume changes. Importantly, prior

work has identified TYMS as a modulator of temozolomide resistance and HMGB2 as a modulator of radioresistance in GBM [79, 81]. In addition, M15 is the target of well established chemotherapeutic agents Aclarubicin, Daunorubicin, Gemcitabine and Doxorubicin, in addition to the antioxidant dietary supplement Quercitin, which has shown promising results in GBM [83] (Fig 4D). In summary, M15 demonstrates a pathway of dysregulated cellular growth and survival with mechanisms promoting resistance to standard therapy, that may be targeted through antioxidants and alternative chemotherapeutic agents.

M16 pathway enrichment is primarily for Alzheimers and related amyloid-beta plaque formation (Fig 4C). Close inspection of M16 hub genes (Fig 4H) highlights genes CLU and CST3, which though related to these pathways are also implicated in several GBM roles, including the microglial and astrocytic response to GBM [84, 85, 86, 87, 88]. Further, hub genes CST3, S100B, GFAP, AQP4, and CLU are all markers of the Neftel AC tumor state [39], recapitulating results of Figure 2H and S1F where the Neftel AC-like state coincides with CT spots. Hub genes S100B, AHCYL1, METTL7A, SCD5 have been implicated in a variety of GBM roles including immune TME modulation and GSC protection [89, 90, 91, 92]. CLU is further implicated as an important mediator of temozolomide resistance in GBM [93]. Interestingly, M16 was identified as a target of the chemotherapeutic agent Vinblastine (Fig 4D). Together these suggest an immune response modulating, GSC protecting, Neftel AC-like niche that promotes temozolomide resistance, but may be targeted through Vinblastine.

M13 is enriched for glial differentiation, negative regulation of neuron differentiation, neural vascular, and Na+ ion transmembrane transport pathways (Fig 4C). M13 hub genes (Fig 4H) MLC1, PON2, GATM, EDNRB, TTYH1 and ATP1B2 are marker genes of the Neftel AC state [39], again recapitulating findings in Figure 2H and S1F showing Neftel AC-like state and CT spot overlap. Interestingly, MLC1, ITGB8, and ATP1B2 have been identified as upregulated in GSCs, with ATP1B2 upregulation maintaining GSC survival and MLC1 promoting GSC proliferation and invasion [94, 95, 96]. Hub genes ITGB8, EDNRB, and GATM were identified as hypoxia response genes with diverse roles in GBM including VM formation, vascular regulation, and tumor growth [95, 97, 98]. Further, GATM also acts to maintain the GSC phenotype through creatine metabolic pathways under hypoxic stress [98]. M13 hub gene PON2 has been identified as a target of valproic acid (VPA), playing a central role in reactive oxygen species (ROS) regulation that is acted up on by VPA leading to increased ROS production and GBM growth inhibition [99]. Together these highlight a GSC promoting, hypoxia driven, Neftel AC-like niche with potential vulnerability to VPA.

After integrating spatial and SC LR analyses for CT and filtering for cell types, we obtained 36 interacting pairs. We included both CT and MVP enriched cell types, as vascular proliferation is often embedded within the CT and key signaling could occur at the edge, with the receiver cell type within CT or MVP. Figure 4E shows CellChat [100] statistics for these pairs, ordering the pairs first by unique spatial association with CT followed by CT coefficient - the first 6 pairs in the figure are unique to CT. Considering both spatial coefficients and CellChat communication scores, interactions of interest in CT are AREG-EGFR and ECM-CD44 signaling (collagen and laminin ligands). When evaluating the functional role of these pairs, we discover these pairs are associated with differentially expressed modules in the CT - specifically, AREG-EGFR is associated with module M8 and both collagen/laminin interactions with CD44 are associated with module M14 (Fig 4F). After identifying positive module associations for top 8 LR pairs in CT and ranking modules by the number of pairs they are associated with, M14 and M8 were in the top 5 (S3A Fig). We validate the M14 and M8 associations with these pairs through spatial maps of sample 1512-A, as it has the CT region clearly defined (Fig 4G). We use commot [101] to plot sender statistics for LR pairs; ie, the most likely ligand signal direction proposed by commot.

EGFR is typically involved in normal cell growth and development, and its behavior as an oncogene is well known. In gliomas and across cancers, overexpression or mutation of this protein leads to context-dependent oncogenic behavior, promoting uncontrolled cell proliferation and tumor growth through the activation of several downstream pathways such as PI3K, MAPK, and STAT3 [102, 103, 104]. These pathways may be activated through increased ligand production or receptor mutation, where known ligands include AREG [104]. A recent study by Chen et al proposed the role of tumor associated monocytes (TAMo's) in driving mesenchymal transformation of tumor cells through the AREG-EGFR signaling axis [105]. In contrast to these findings, our CellChat analysis does not implicate TAMs as the primary source of AREG. Instead, the AREG-EGFR interaction in our data is most likely mediated by DC, Mast, or NK cells, targeting OPC-like or AC-like tumor states. Additionally, AREG-EGFR is associated with M8, a module characterized by glial cell differentiation and an OPC-like tumor state (Fig 4F). This suggests a potentially distinct role for EGFR signaling in supporting or reinforcing an OPC-like tumor phenotype, rather than promoting MES transition. While there are no GBM-specific studies indicating this role, literature supports EGFR in OPC specification, and AREG favoring differentiation downstream signaling in a variety of cell types after binding to EGFR [106, 107]. Based on these observations, we hypothesize that in the CT, immune cell–derived AREG may promote or stabilize OPC-like differentiation in AC-like/OPC-like tumor state cells through EGFR activation.

Both laminin and collagen are ECM components; thus their interaction with CD44 in normal tissue is primarily to maintain tissue structure [108]. In GBM, our top collagen (COL6) protein has been found significantly upregulated in GBM and strongly correlates with the stem-like phenotype [109, 110]. While laminin has less literature support, one study indicates the role of laminin alpha-2 in stem cell maintenance in GBM [111]. CellChat indicates both top collagen and laminin pairs most likely

interact between Mural Cells and AC-like tumor state, and both interactions are associated with M14, a module characterized by GSC program activation (Fig 4F). Thus, we can hypothesize that ECM interactions with CD44, our top ligands being COL6A3 and LAMC3, promote glioma stem cell maintenance in AC-like tumor states in the CT.

We further performed direct modeling of LR spatial co-expression as a function of all DE genes, followed by pathway enrichment of significantly associated gene sets (S4 Fig). For CT pairs, AREG-EGFR associated genes are enriched for positive regulation of PI3K transduction, supporting immediate downstream activity of this pair as previously described. We also identify laminin and collagen pairs associated with genes enriched for supramolecular fiber organization, supporting the normal role of these interactions in tissue structure maintenance.

Integrin and immune (GZMA-F2R) signaling promote angiogenesis and anti-tumor behavior respectively in the perivascular niche

The microvascular proliferation niche consists of central areas of blood vessel formation, including new vessels and branches from existing vessels, known to play a significant role in tumor growth and vascularization.

One-vs-all differential ME expression analysis identified 5 upregulated modules in the MVP region relative to the rest of the tumor sample. In order of decreasing LFC these are: M7, M5, M17, M2 and M15 (Fig 5A). M7, M5, and M17 were shown by linear mixed effect modeling of ME values by IVY region assignment to be upregulated in the MVP region compared to the LE, CT, and PAN regions. In contrast, M2 is upregulated in the MVP region relative to the LE and CT regions, with no significant difference in expression relative to the PAN region. M15 is upregulated in the MVP region relative to the PAN and LE regions, but is downregulated in relation to the CT region (Fig 5B).

Figure 5. MVP-specific pathway and LR analysis. (A) One-vs-all testing of MEs in MVP relative to the rest of the tumor. Circles marked "x" where FDR > 0.05. (B) Coefficients from mixed effect modeling of ME against IVY region assignment, ME change shown in relation to MVP level. "*" where FDR < 0.05. (C) Top pathway terms for 5 most upregulated modules in the MVP. (D) Top drugs by significance of gene target enrichment for 5 most upregulated modules in MVP. (E) CellChat communication scores for top LR pairs whose spatial co-expression is associated with MVP. Note, as score is dependent on expression values, scoring is relative across cell type combinations and LR pairs. (F) T-values from lr-module regression specific to MVP LR pairs. Modules shown are differentially expressed in MVP. (G) Spatial plots of IVY region assignment and select LR coexpression and ME scores. (H) Network visualization of top 10 hub genes for the 5 most upregulated modules in MVP.

Term enrichment analysis of M7 highlights its distinct role in angiogenesis and extracellular matrix organization, consistent with defining features of the MVP region (Fig 5C). In addition, of the upregulated modules in the MVP region, M7 is the most highly enriched for the epithelial-mesenchymal transition (EMT) pathway. At the hub of M7 (Fig 5H), we identify the ECM related genes FN1, COL3A1, COL4A1, COL4A2, COL18A1, and ITGA1 which have had key roles identified in GBM including vascularization, EMT, invasion, and worsened prognosis [112, 113, 114, 115, 116, 117]. Importantly, the M7 hub genes TAGLN, NOTCH3, and ITGA1 have been identified in prior work for their critical involvement in GBM resistance to temozolomide, a first-line anti-cancer therapy in the management of GBM [117, 118, 119, 120]. However, the M7 hub gene FN1, which has been identified as an essential gene in GBP2-driven invasion [112], may also present a novel therapeutic target [121, 122]. Together, M7 demonstrates a ECM related pathway of EMT, tumor invasion, and temozolomide resistance, which may be targetable through the FN1 hub gene.

Term enrichment analysis of M5 highlights an upregulated inflammatory immune response within the MVP (Fig 5C). Increased expression of M5 hub genes (Fig 5H) including FCER1G, CD74, C1QA, C1QB and C1QC have been associated with worsened prognosis in GBM [123, 124, 125], while C3 has been identified as a promoter of GBM growth and aggressiveness [23]. Together these indicate that M5 represents a heightened, though ineffective or even counterproductive inflammatory immune response in the MVP region.

Term enrichment of M17 highlights functions related to apoptosis and NF-kB signaling (Fig 5C). M17 hub genes (Fig 5H) including NF-kB regulated AP-1 complex proteins (FOS, FOSB, and JUNB), IER2, and MCL1 have been identified in prior work for promoting GSC and GBM cell survival and proliferation [126, 127, 128, 129, 130, 131]. For MCL1, this role has been linked to bortezomib therapy resistance [131]. In contrast, DUSP1 and ZFP36 have been shown in prior work to promote GSC differentiation and decrease GBM cell viability respectively [132, 133]. Together, M17 may represent a niche where signals compete in the MVP to maintain GSC and GBM cell survival. Interestingly, drug target enrichment identifies alitretinoin as a potential therapy targeted towards M17 (Fig 5D) and retinoic acids have been highlighted in prior work on novel GBM therapies specifically for their role in differentiating GSCs and reducing GBM cell viability [134, 135, 136, 137].

After integrating spatial and SC analyses for MVP and filtering for cell types, we obtained 114 interacting LR pairs. We included both CT and MVP enriched cell types, as vascular proliferation is often embedded within the CT and key signaling

could occur at the edge, with the receiver cell type within MVP or CT. Figure 5E shows CellChat statistics for the top 11 pairs uniquely co-expressed in MVP, ordering the pairs by spatial modeling coefficient. Considering both spatial coefficients and CellChat communication scores, interactions of interest include integrin signaling (COL4A1-ITGA1-ITGB1), GZMA-F2R, and PTN-PRPZ1. When evaluating the functional role of these pairs, we discover these pairs are associated with network modules differentially expressed in MVP. Namely, integrin signaling is strongly associated with M7, GZMA-F2R is associated with M5, and PTN-PTPRZ1 is associated with both M7 and M17 (Fig 5F). After identifying positive module associations for the top 15 LR pairs in MVP and ranking modules by the number of pairs they are associated with, M7, M17, and M5 were in the top 5 (S3B Fig). We validate the M7 and M5 associations with these LR pairs through spatial maps of both samples 1512-A and 8379-2, as the MVP region is generally smaller than others and both these samples have the region clearly defined (Fig 5G). We use commot to plot sender statistics for LR pairs.

Integrin signaling is consistently activated in the MVP region by different ECM-ligands including collagen, FN1, laminin, and POSTN. In normal tissue, this family of signaling allows physical cell-cell and cell-ECM connectivity, maintaining cell shape, migration, and cell cycle progression [138]. In GBM, many studies identify the critical pro-angiogenic role of integrins, discovering high expression of these receptors on endothelial cells [139, 140]. Consistent with this, we see that the highest CellChat communication scores for integrin signaling are between non-tumor cells; specifically autocrine mural cells or mural - endothelial cells (S5 Fig), likely providing a scaffold for endothelial cell migration when branching out to create new vessels. We also see the associated module, M7, is characterized by ECM organization and Angiogenesis (Fig 5C). However, we note among all tumor-specific interactions, COL4A1-ITGA1-ITGB1 (along with FN1 and LAMC3 pairs) is most likely interacting between Mural and OPC-like cells. While less widely studied, an integrin-driven increase in tumor invasive properties has been identified in GBM [141]. Thus, from our analysis we can strongly support angiogenesis driven by integrin signaling on endothelial and mural cells in MVP, and further hypothesize that tumor migration at the CT-MVP edge is promoted by integrin activation via mural cells.

GZMA is a protein found in NK cells and cytotoxic T cells, playing a role in target cell death [142]. While studies on the GZMA-F2R interaction are limited, a recent study proposed its anti-tumorigenic role in hepatocellular carcinoma (HCC), specifically revealing GZMA secreted by the T cells interacted with F2R expressed by tumor cells to induce T-cell mediated tumor suppression via activation of JAK2/STAT1 pathway [143]. In our analysis, CellChat indicates among tumor state interactions, this pair most likely interacts between CD4/8 or NK cells as sender, and AC-like or OPC-like tumor states as receiver. Additionally, the associated module M5 is characterized by positive regulation of cytokine production, phagocytosis, and apoptosis (Fig 5C). From this, we strongly hypothesize GZMA-F2R signaling between immune cells (NK and T cells) and tumor states promotes anti-tumorigenic behavior in the MVP region.

In normal brain tissue, the PTN-PTPRZ1 interaction plays key roles in neural development, including the development and survival of outer radial glia (orG); however, this pair is found overexpressed in GBM [144]. Several studies identify this LR interaction between TAM's and glioma stem cells (GSCs) by showing that silencing PTN expression in TAMs mitigates their pro-tumorigenic activity [145, 146]. These studies reveal PTN binding to PTPRZ1 allows the GSCs to self-renew and maintain stem-like properties. However, CellChat indicates this LR pair most likely interacts between AC-like and OPC cells from our SC data, suggesting an alternative signaling route in the MVP region. In recent works, PTPRZ1 was identified as a marker gene for an OPC enriched transcriptomic cluster, specifically emphasizing the expression of PTPRZ1 along the orG differentiation to OPC cells in GBM [147, 148]. While there is no direct literature on PTN presence in AC-like tumor state, studies indicate this protein is expressed by GBM tumor cells as well as TAMs [149]. Additionally, we note the associated module M7 is enriched for EMT (Fig 5C). Thus, we hypothesize PTN-PTPRZ1 signaling between AC-like tumor state and OPC cells promotes the maintenance of stem-like properties in specifically OPC cells in the MVP region.

We further performed direct modeling of LR spatial co-expression as a function of all DE genes, followed by pathway enrichment to support LR-module associations (S4 Fig). For MVP pairs, both integrin signaling and PDGFB-PDGFRB associated genes are enriched for blood vessel development and ECM organization, supporting the role of these pairs in angiogenesis. We note that while blood vessel development/angiogenesisis enriched for pairs across CT, MVP, and PAN, the highest z-score is for MVP-specific pairs.

MIF-CD74/CXCR4 and FN1/SPP1-CD44 signaling promotes inflammatory response through immunosuppression and EMT in the PAN region

The pseudopalisading niche consists of tumor cells migrating from necrotic centers due to hypoxia, resulting in distinct histological and molecular patterns around these centers promoting vascularization and inflammatory response.

One-vs-all differential ME expression analysis revealed 4 upregulated modules in the the PAN region relative to the rest of the tumor sample. Listed in order of decreasing LFC these are M4, M2, M5, and M17 (Fig 6A). Of note, linear mixed effect modeling of ME values by IVY region assignment shows only M4 expression is increased in PAN relative to CT, MVP, and LE regions (Fig 6B). M2 is overexpressed in the PAN region relative to the CT and LE regions, with no significant change in

expression relative to MVP. M5 and M17 however, are most overexpressed in the MVP region (Fig 6B). Given these expression patterns, we will limit our focus to M4 and M2 in this section.

Figure 6. PAN-specific pathway and LR analysis. (A) One-vs-all testing of MEs in PAN relative to the rest of the tumor. Circles marked "x" where FDR > 0.05. (B) Coefficients from mixed effect modeling of ME against IVY region assignment, ME change shown in relation to PAN level. "*" where FDR < 0.05. (C) Top pathway terms for 5 most upregulated modules in the PAN. (D) Top drugs by significance of gene target enrichment for 5 most upregulated modules in PAN. (E) CellChat communication scores for top LR pairs whose spatial co-expression is associated with PAN. Note, as score is dependent on expression values, scoring is relative across cell type combinations and LR pairs. (F) T-values from lr-module regression specific to PAN LR pairs. Modules shown are differentially expressed in PAN. (G) Spatial plots of IVY region assignment and select LR coexpression and ME scores. (H) Network visualization of top 10 hub genes for the 5 most upregulated modules in PAN.

Enrichment analysis of M2 and M4 highlights their similar functional pathways involving GBM specific genes responding to hypoxic stress, fitting consistently with their upregulation in the PAN region (Fig 6C). Compared to M2, M4 is uniquely enriched for negative regulation of lipase activity (S7 Table). M4 hub genes (Fig 6H) HILPDA, ADM, NDRG1, AKAP12, SLC2A1, and ANGPTL4 are markers for the Neftel MES2 tumor state [39], recapitulating findings in Figure 2H and S1F showing MES2-like overlap with PAN spots. Hub genes VEGFA and LOX modulate the immune TME to protect GBM cells [150, 151]. Hub gene ANGPTL4 drives GSC enrichment [152]. NDRG1 has been shown to play a key role in driving vasculogenic mimicry [153]. SLC2A1 and ADM have been identified as key glycolysis-related genes in cancer prognosis, with ADM highlighting a potentially targetable pathway in glioma [154, 155]. HILPDA has been shown to be central to PAN region specific lipid droplet accumulation, GBM cell state related lipid metabolism modulation, and a potential therapeutic target in GBM [156]. Importantly, ADM, ANGPTL4, SERPINE1/VEGF, and CA12 have been identified as actionable targets to overcome temozolomide resistance [152, 157, 158, 159]. Additionally, AKAP12 has been identified as a biomarker of resistance to VEGF targeted therapy [160]. Together, M4 represents an MES2-like niche related set of pathways responding to hypoxic stress that promotes therapeutic resistance through multiple mechanisms. Further, M4 is a target of arsenic trioxide (Fig 6D), a chemotherapeutic agent capable of crossing the blood brain barrier with some promise for GBM therapy [161, 162].

Compared to M4, M2 is more enriched for genes related to the regulation of apoptosis, inflammation, and EMT pathways (Fig 6C). M2 hub genes (Fig 6H) ANXA2, VIM, TIMP1, TAGLN2, and TUBA1C are markers of the Neftel MES1 tumor state [39], reinforcing findings from Figure 2H and S1F showing MES1-like overlap with PAN spots. Further TAGLN2 is noted in GBM for promoting proneural-mesenchymal transition [118]. Hub genes ANXA2, TIMP1, TUBA1C have been highlighted in previous literature for their roles in shaping the immune TME of GBM [163, 164, 165]. TNFRSF12A, FLNA, VIM, IGFBP2, and CD151 are related to GBM cell motility, a critical feature within the PAN region, with related importance to invasion and prognosis [166, 167, 168, 169, 170]. Additionally, IGFB2 has been shown to promote vasculogenic mimicry in GBM [171]. Temozolomide resistance is noted in relation to M2 hub genes as well, including with TAGLN2, IGFBP2, and CD63/TIMP1 [118, 169, 172]. Altogether, M2 represents an MES1-like niche related to important processes modulating the immune TME, hypoxic stress responses, and temozolomide resistance.

After integrating spatial and SC analyses for PAN, we obtained 13 LR pairs interacting between PAN tumor states and other cell types abundant to PAN. Figure 6E shows CellChat statistics for these pairs, ordering the pairs first by uniqueness to region followed by spatial modeling coefficient. Considering both spatial coefficients and CellChat communication scores, interactions of interest include specific CD44 signaling (SPP1-CD44, FN1-CD44) and MIF-CD74/CXCR4. We note that FN1-CD44 and SPP1-CD44 have a significant association with both PAN and LE regions, where SPP1-CD44 has a much larger coefficient for PAN and FN1-CD44 has similar coefficients for both regions. However, FN1-CD44 is not identified to have a strong signal between tumor-state specific interactions in LE; thus, we can infer it primarily functions in the PAN niche. Additionally, we identify MIF-CD74/CXCR4 coexpression in both PAN and CT regions from our modeling; however, the coefficient for PAN is much greater, allowing us to consider this pair primarily interacting in the PAN niche. When evaluating the functional role of these pairs, we discover these interactions are associated with network modules differentially expressed in PAN. Namely, MIF-CD74/CXCR4 is strongly associated with M4, and the 2 CD44 signaling pairs are associated with both M4 and M2, but have a higher t-statistic for M2 (Fig 6F). After identifying positive module associations for all pairs in PAN and ranking modules by the number of pairs they are associated with, M4 and M2 were in the top 5 (S3C Fig). We validate the M2 and M4 associations with these LR pairs through spatial maps of sample 1512-A, as it has the PAN region clearly defined (Fig 6G). We use commot to plot sender statistics for LR pairs.

MIF is a cytokine that can bind to both CD74 and CXCR4 as a complex, typically triggering leukocyte modulation and recruitment [173]. Aligned with this, CellChat indicates this pair most likely interacts between MES-like and Monocytes. Literature indicates in GBM as well as other cancers, MIF-CD74 axis acts through immune suppression, modulating classi-

cal/alternative polarization of Monocytes [174, 175, 176]. However, the role of MIF in GBM is complex, presenting both anti and pro-tumorigenic effects depending on the context [177]. The over-expression of MIF in response to hypoxic stressors has been shown in several studies [178, 179]. In 2017, Guo et al proposed hypoxia-induced vascular mimicry (VM) formation through the CXCR4-AKT-EMT pathway driven by MIF [179]. Unlike angiogenesis which relies on endothelial cells, VM involves tumor cells directly forming blood vessels/channels. In our analysis, MIF-CD74/CXCR4 is strongly associated with M4 which is enriched for vessel formation functions, supporting the hypothesis that VM is driven by this MIF pair in response to hypoxia. Thus, we present two strong roles of this MIF interaction in response to hypoxia - both immune suppression and promoting blood vessel formation.

The interactions of both FN1 and SPP1 with CD44 are typically involved in cell processes during wound healing, unlike the ECM component interactions with CD44 identified in CT, whose primary role is tissue integrity [180]. Literature reveals that macrophage signaling in GBM, as well as several other cancers including liver and ovarian metastases, via the SPP1-CD44 axis drives T cell exhaustion and therefore contributes to immunosuppression [181, 182, 183]. However, in our data from Figure 6E, CellChat indicates these CD44 interactions in the PAN region are most likely between Monocytes and MES-like tumor states, as T cells are not enriched in this region. Additionally, the spatial co-expression of both CD44 pairs are associated with module M2 in our analysis. When compared to the other PAN-specific modules, M2 is characterized by inflammatory response and EMT. Supporting an alternative mechanism of SPP1-CD44 interaction in high-grade glioma, in 2021 He et al. proposed that this interaction plays a critical role in macrophage-mediated induction of MES-like tumor state [184]. Thus, we hypothesize a niche regional mechanism of these CD44 pairs, particularly SPP1-CD44, in driving MES-like tumor state induction in the PAN region through macrophage-tumor signaling.

We further performed direct modeling of LR spatial co-expression as a function of all DE genes, followed by pathway enrichment of significantly associated gene sets. For PAN pairs, response to hypoxia and wound healing is enriched across pairs, supporting inflammatory response to oxygen deprivation in PAN (S4 Fig). Interestingly, we identify that the intrinsic apoptotic signaling pathway in response to DNA damage is enriched for genes associated with MIF-CD74/CXCR4, previously shown to be involved in immunosuppression (and angiogenesis). Thus, this LR interaction could be a response to DNA damage in order to support cell survival.

Ephrin signaling drives neuronal guidance of tumor invasion in LE

The leading edge (LE) consists of the TME at the end of the infiltrative spectrum. Here, tumor cells have migrated away from CT to infiltrate normal tissue in order to escape hypoxia and maintain metabolism.

One-vs-all differential ME expression analysis revealed 6 upregulated modules in the LE relative to the rest of the tumor sample, with the top 5 in order of LFC being: M3, M11, M19, M18, and M6 (Fig 7A). In addition, linear mixed effect modeling of ME values by IVY region assignment showed increases in M3 and M19 expression relative to CT, MVP, and PAN regions. In comparison, M11, M18, and M6 are upregulated relative to MVP and PAN regions, but are downregulated or expressed at similar levels relative to CT (Fig 7B).

Figure 7. LE-specific pathway and LR analysis. (A) One-vs-all testing of MEs in LE relative to the rest of the tumor. Circles marked "x" where FDR > 0.05. (B) Coefficients from mixed effect modeling of ME against IVY region assignment, ME change shown in relation to LE level. "*" where FDR < 0.05. (C) Top pathway terms for 5 most upregulated modules in the LE. (D) Top drugs by significance of gene target enrichment for 5 most upregulated modules in LE. (E) CellChat communication scores for top LR pairs whose spatial co-expression is associated with LE. Note, as score is dependent on expression values, scoring is relative across cell type combinations and LR pairs. (F) T-values from lr-module regression specific to LE LR pairs. Modules shown are differentially expressed in LE. (G) Spatial plots of IVY region assignment and select LR coexpression and ME scores. (H) Network visualization of top 10 hub genes for the 5 most upregulated modules in LE.

M3 is enriched for pathways related to neurotransmission, neuron projection development and glutamate metabolism (Fig 7C). This recapitulates our findings from differential expression and TF module analysis showing increased neuronal signaling and synaptic activity in the LE. M3 hub genes (Fig 7H) STMN2, SNAP25, and GNG3 associate this module with the Neftel NPC2 tumor state [39], recapitulating findings from Figure 2H and S1F showing NPC2-like overlap with LE spots. Hub genes SNAP25, ATP1A3, VSNL1, SLC17A7, and NRGN have been identified in prior work for inhibiting the growth and spread of GBM, with SNAP25 notable for accomplishing this through regulation of glutamate metabolism [185, 186, 187, 188, 189, 190]. STMN2 promotes axonal outgrowth and regeneration [191]. Interestingly, ENC1 upregulation is a marker of poor prognosis in GBM and has been implicated as a cancer promoter [192]. Taken together, M3 encapsulates an NPC2-like niche possessing both tumor inhibiting behavior and mechanisms that may continue to promote the growth and spread of GBM.

M6 overlaps in functionality with M3 but is more specifically related to glutumate and aspartate transmembrane transport (S7 Table), lacking enrichment for neuron projection development. M6 hub genes (Fig 7H) SLC1A3, ATP1A2, and NDRG2

associate M6 with the Neftel AC tumor state [39]. Importantly, altered glutamate and aspartate related pathways have been shown to influence GBM and GSC proliferation, invasion, and TME immune evasion [193, 194]. Further, we note that M6 is upregulated in CT relative to LE (Fig 7B). As such, M6 may represent dysregulation of glutamate/aspartate pathways in transition from LE to CT promoting an AC tumor state, or inversely, a process being utilized by tumor cells in transition from CT to LE.

M19 is enriched for genes related to neuron differentiation and EMT pathways (Fig 7C). The top 10 M19 hub genes (Fig 7H) are all mitochondrially encoded genes, potentially indicating contamination from cell death. However, recent literature has indicated that in the context of cancer tissue research this may represent meaningful biological signal in relation to metabolic regulatory alterations [195]. This latter interpretation is reinforced by our findings from TF module analysis showing increased mitochondrial activity in the LE. In addition, mitochondrially encoded gene expression has been found to be inversely correlated with WHO glioma grade and the M19 hub genes MT-ATP6, MT-CO3, MT-CYB, MT-CO2, and MT-ND4L have been positively correlated with improved prognosis in glioma [196]. Additional M19 genes (S6 Table), a 29 gene module, including SRCIN1, TMEFF2, and ANK3 are found to be negatively correlated with GBM diagnosis, proliferation or invasion [197, 198, 199, 200]. In contrast, SEC62 upregulation has been linked with tumor cell invasion [201], SPOCK1 with temozolomide resistance [202], and IGSF8 with tumor cell immune system evasion [203]. MAP1B, NTM, and FAM171A1(astroprincin) are related to axonal growth, neurite outgrowth, and astrocyte projection development respectively [204, 205, 206]. Taken together, M19 represents pathways related to a transition towards normalcy from the GBM state associated with underlying mechanisms that may continue to promote the growth and spread of GBM cells. Of note, M19 is enriched for targets of metformin (Fig 7D), which has been receiving significant attention for it's potential role in a variety anti-cancer therapies including GBM [207, 208, 209].

After our integrative spatial and SC analysis for cell communication inference, we obtained 21 LR pairs interacting between LE tumor states and other cell types abundant to LE. Figure 7E shows CellChat statistics for these pairs, choosing 2-3 pairs per signaling family and ordering the pairs first by uniqueness to region followed by spatial modeling coefficient. Considering spatial coefficient order and CellChat communication scores, top interactions of interest include ephrin signaling, CNTN2-CNTN2-CNTNAP2, and CNTN1-NRCAM. From literature, these top pairs are focused on different aspects of neuronal development, including axon guidance (ephrin signaling) and synaptic growth and maintenance (others) [210, 211]. When investigating the data-driven functional role of these pairs, we identify that these top interactions are strongly associated with network modules differentially upregulated in LE. Specifically, ephrin signaling is strongly associated with module M3, and CNTN2-CNTN2-CNTNAP2 with M6 (Fig 7F). After identifying positive module associations for the top 7 pairs in LE and ranking modules by the number of pairs they are associated with, M3 was in the top 5 (S3D Fig). We validate the M3 and M6 associations with these LR pairs through spatial maps of sample 8279-2, as it has the LE region clearly defined (Fig 7G). We use commot to plot sender statistics for LR pairs.

Ephrin signaling is involved in axonal guidance and cell migration during healthy neuronal development [211]. Consistent with this, CellChat results indicate the strongest ephrin pair, EFNB3-EPHB6, is most likely interacting between NPC-like and neuron cells. However, in GBM, ephrin interactions have a complex role, with some promoting tumor-suppressive behavior such as EphA1 and EphA5, while many promote aggressive invasion particularly along white matter tracts such as EphA2, EphA3, and EphB3 [212, 213]. Our top identified ephrin pairs include EphA2 and EphB3. Thus, our discovery of ephrin-M3 association supports the role of ephrin signaling in promoting tumor invasion through neuronal guidance, and we can hypothesize the top driving pair EFNB3-EPHB6 interacting between NPC-like and neuron cells.

CNTN2-CNTN2-CNTNAP2 also supports neuronal development by forming a synaptic bridge, particularly at the nodes of Ranvier where this interaction maintains the presence of voltage-gated potassium channels and therefore proper nerve conduction [214]. Consistent with this function, CellChat suggests this pair most likely interacts between NPC-like and neurons. However, loss of CNTNAP2 has been suggested to negatively affect intracellular GluA1 (glutamate receptor) transport and glutamate uptake in mice, indicating CNTNAP2 is involved in the proper localization of these receptors [215]. This strongly supports the specific functional enrichment of module M6 for glutamate transport while maintaining activation of neuronal development in the LE. While the specific CNTN2-CNTN2-CNTNAP2 interaction has not been identified in GBM literature, from our analysis we can hypothesize this signaling from NPC-like to neurons plays an important role in LE-specific functions, specifically glutamate transport.

We further performed direct modeling of LR spatial co-expression as a function of all DE genes, followed by pathway enrichment of significantly associated gene sets. For LE pairs, neuron projection is enriched for ephrin signaling associated genes as expected (S4 Fig). Additionally, we identify cholesterol/sterol homeostasis and transport enriched for CNTN2-CNTN2-CNTNAP2 associated genes, where glutamate can trigger changes in cholesterol distribution, providing a nuanced pathway consistent with our previous hypothesis [216].

Discussion

In this work, we systematically resolved the spatial complexity of GBM by jointly analyzing a large cohort of ST slides using a range of computational pipelines. Our analyses reveal that distinct anatomical niches within GBM impose unique gene regulatory programs on tumor cells, resulting in marked differences in transcriptional states and cellular compositions across regions. We further leveraged a spot deconvolution algorithm to extract tumor-specific expression profiles from our ST slides [42], enabling robust dissection of malignant cell programs despite microenvironmental admixture. The resulting data faithfully recapitulated established spatial trends in GBM biology, including the niche-specific enrichment of canonical gene modules such as those described by [39], with distinct transcriptional states mapping to perivascular, hypoxic, and invasive regions. Comparative analysis of tumor cell expression across these niches revealed extensive gene expression changes, consistent with the well-documented association between spatial microenvironments and GBM cell state heterogeneity [8, 9].

By integrating all slides into a unified low-dimensional embedding, we identified TF modules exhibiting highly localized spatial activity. Several TF modules were specifically active in the perivascular niche, each associated with discrete biological processes, while others were restricted to the LE or PAN regions. Notably, we discovered two TF modules with activity concentrated along niche interfaces: one at the CT-PAN boundary, enriched for metabolic adaptation to hypoxia, and another at the CT-LE interface, strongly associated with RNA splicing and isoform diversity, an emerging hallmark of tumor invasiveness in GBM [52]. Importantly, the activity of these 9 TF modules varied across individual slides, reflecting the limited and heterogeneous spatial sampling inherent to each tissue section. This underscores the necessity of pooling data across a large, representative cohort to comprehensively capture the spatial regulatory landscape of GBM [9, 12]. Our integrative approach, leveraging a unified data embedding, provides a powerful framework for studying spatially resolved gene regulatory programs and uncovering novel mechanisms of tumor adaptation in GBM.

In addition, we spatially characterized molecular pathway reprogramming using ST GCN modules produced through hdWGCNA [13]. Our GCN modules reinforce and are reinforced by established spatial patterns of biological pathway activity in GBM. They highlight region specific associations for Neftel tumor states including: CT with AC-like, OPC-like and NPC-like states; LE with the NPC2-like state; and PAN with the MES1-like and MES2-like states. Further, they place independently studied GBM related genes into spatial functional contexts based on their hub gene status within modules and their assigned module's association with Ivy GAP niches. Importantly, for each region we are able to identify at least 1 pathway enriched for a drug or drug class with promising evidence in the GBM literature, along with numerous pathway specific module hub genes that have been proposed as targets for therapy or are important mediators of therapy resistance.

Intercellular communication and molecular pathway reprogramming are niche-specific in GBM, with major impacts on disease progression, invasion, and therapeutic response. Thus, we spatially characterized cell communication between malignant and non-malignant cell types through a novel integrative workflow combining SC and ST analysis. Further, we related the spatial patterning of intercellular communication and GCN module defined pathway reprogramming to identify novel and established mechanisms driving functional niche characteristics. In the CT, we identify the localization of the AREG-EGFR axis mediated by immune cells and targeting AC-like/OPC-like tumor states. The role of this pair in GBM, particularly in MES transformation, is strongly supported by literature [105]. However, our CellChat analysis proposes a novel role for this pair, specifically immune-mediated OPC-differentiation or maintenance of AC-like/OPC-like tumor states, as evidenced by the pair's association with glial differentiation and the OPC-like tumor state. We also discover ECM-CD44 interactions, likely to promote GSC program activation from their association with NPC1-like state associated GSC proliferation and maintenance. In MVP, we identify dual roles of LR signaling - namely pro-metastatic through angiogenesis driven by integrin signaling, and anti-tumorigenic driven by immune signaling via GZMA-F2R. These interactions are novel in GBM, offering insight into niche-specific mechanisms of metastasis and immune signaling. We identify a significant association between GZMA-F2R signaling and an inflammatory immune response with an apparently complex role in GBM, as many of its hub genes are associated with worsened prognosis in GBM. In addition, we identify a significant association between COL4A1-ITGA1-ITGB1 signaling and angiogenesis and related ECM organization in addition to the EMT pathway. In PAN, we uncovered spatially patterned mechanisms of the inflammatory response, including immunosuppression, and MES-like state transition, driven specifically by MIF signaling and FN1/SPP1-CD44 interactions. MIF signaling is proposed to have a complex role in GBM, and our analysis specifically supports the role of MIF signaling in vascular mimicry [174, 179]. MIF-CD74-CXCR4 signaling is significantly associated with an MES2-like state, hypoxia and glycolysis pathways that includes the hub gene NDRG1, a driver of vasculogenic mimicry [153]. FN1-CD44 signaling is significantly associated with an MES1-like state, inflammation and the EMT pathway. Finally in LE, we identified literature-supported ephrin signaling driving neuronal guidance and supporting tumor invasion. Further, we hypothesized the novel LE-dominant role of CNTN2-CNTN2-CNTNAP2 in promoting glutamate and fatty acid transport. We identify ephrin signaling as associated with the NPC2-like tumor state and enriched for neuron projection pathways. In addition, we identify NTN2-CNTN2-CNTNAP2 signaling with glutumate and aspartate transmembrane transport, whose dysregulation appears closely related with the AC-like tumor state.

Despite these advances, some limitations remain. The resolution of Visium spatial profiling constrains our ability to pinpoint

tumor-specific expression changes at SC resolution, and our deconvolution depends on the breadth and quality of available SC references. We also have not fully characterized the dynamic states of immune and stromal cells across niches. Recent studies have highlighted extensive immune rewiring in the GBM ecosystem [217] and the important functions of cancer-associated fibroblasts in tumor growth and treatment response [218]. Future work employing higher-resolution spatial profiling will be crucial for unraveling the full complexity of the tumor microenvironment and understanding how spatial context shapes cell states. In addition, further work designed to explore the temporal nature of these niche characteristics, including their response to treatment and transformations during recurrence, will shed further light on our findings' clinical implications.

Our findings have direct therapeutic implications. The remarkable diversity of cell states within a single tumor likely explains the limited efficacy of single-agent therapies, such as EGFR or VEGF inhibitors. This work underscores the urgent need for rational combination therapies that can simultaneously target key vulnerabilities or master regulators within each tumor niche. Embracing the spatial and functional heterogeneity of GBM will be essential for developing more effective and durable treatment strategies for this devastating disease.

Methods and Materials

Sample Collection

Tumor samples used for Visium ST were obtained from patients undergoing tumor resection at the University of Michigan Hospital by Prof. Al Holou. fourteen tissue sections were collected in house from n=7 patients. Five slides included adjacent sections of the same tumor tissue, and slides 1512-A/B and 1512-C/D were collected from different regions of the same tumor. Eight slides are primary tumor, while six (5492-C/D, 8379-A/B/C/D) were from recurrent GBM.

Visium data for the Freiburg cohort were downloaded from DRYAD (https://datadryad.org/dataset/doi:10.5061/dryad.h70rxwdmj), and the Broad Institude cohort was downloaded from zenodo (https://zenodo.org/records/12624860).

Processing and QC of Visium ST Data

Spots with fewer than 200 expressed genes were labeled as low quality and excluded from downstream analyses. Similarly, spots with over 5% haemoglobin genes were excluded due to excessive bleeding in tissue. Any slide with fewer than 100 spots passing QC thresholds were not used for integrative analysis. Slides passing QC for each cohort were independently merged into a single Seurat object. Counts data analysis was carried out using Seurat v5.2 [219]. Raw counts were normalized using the *NormalizeData* function. Top 3000 variable genes were used for dimension reduction using PCA with the *RunPCA* function, and the top 15 PCs were used to construct the UMAP data embedding using *RunUMAP* for sample visualization in the UM cohort.

Spot-Level Scoring for Genesets

Normalized counts per spot were used to compute enrichment scores for different genesets of interest using the UCell algorithm [15]. This algorithm was specifically developed for dealing with data sparsity in single cell datasets, and uses the non-parametric Mann-Whitney U statistic for robust computation of enrichment scores. Scores are computed using the *AddModuleScore_UCell* function with $maxRank = 3000$. Spot-level niche annotation was carried out by computing enrichment scores for regional markers from the Ivy-GAP study [4], and labeling spots based on maximal scores. The same algorithm is used for computing Hallmark scores per spot, with genesets downloaded using the *msigdbr* package [220]. Enrichment scores for Hallmark signatures were added as a new assay to the merged Seurat object to use for downstream differential analysis and visualization.

Differential Expression Analysis

Differential analysis with genes/ pathway scores were carried out using the *FindAllMarkers* function in Seurat, with the default Wilcoxon Rank-Sum test for the appropriate assay object between conditions of interest. We used significance thresholds of $FDR < 0.05, log2FC > 1$ to identify markers, unless otherwise stated. Enrichment analysis for significantly differential genes was carried out using the *clusterProfiler* R package [221, 222] using the *compareCluster* function.

Visium Spot Deconvolution

Visium spot deconvolution was performed using the BayesPrism [42] algorithm, using a comprehensive GBM single-cell atlas [14] as reference. We used the level-3 annotation from the atlas for celltype/cellstate annotation. We downsampled the atlas to 3000 randomly selected cells per reference group. Raw counts for protein-coding genes from single cell and Visium data were used to create the BayesPrism object. For the inference, we used the InstaPrism algorithm [33], which re-implements the BayesPrism by replacing the Gibbs sampling step with a fixed-point algorithm, providing considerable speed and memory advantages. In addition to spot compositions, we also use the algorithm to extract spot-level tumor-specific expression data for the whole transcriptome, and save this as a new assay in the Seurat object.

Constructing Cell-Interaction Graph

The inferred spot-level cell type compositions from deconvolution are used to construct a cell-cell interaction graph. Since the data is compositional, we use the centered-log ratio (CLR) transform to bring them into Euclidean space, and then use the graphical-lasso algorithm [223] to infer an interaction graph between celltypes. We show all non-zero edges at a sparsity threshold of $\lambda = 1$, since the suggested λ_{min} and λ_{1se} values gave too many interactions.

Learning 2D PCA Embedding To Capture Intrinsic Spatial Context Across Slides

To study how biological processes are continuously changing along spatial gradients, we learned a 2D data embedding that preserves spatial tissue context of every Visium spot across slides. We trained an scVI model on the Visium data across all 44 slides for the whole transcriptome, treating each slide as an independent batch. We used a model with two layers and 30 latent variables, with the negative binomial likelihood for modeling gene expression counts. The trained model was used to generate counterfactual normalized, batch-corrected counts (mapped to reference slide 1512-A) for the Ivy marker genes for all spots across the entire dataset. These batch-corrected counts were used to generate a supervised PCA-embedding for the dataset that captures their relative enrichment for the four distinct tissue niches.

Hotspot Analysis to Identify Co-Expressed TF Modules

We used Hotspot [47] to identify modules of spatially co-expressed TFs (TFs) from the PC embedding. We construct a kNN graph on the PC embedding with k=15 to compute auto/cross-correlation metrics, and use the tumor-specific expression data to identify modules of TFs with spatially localized activity in tumor cells. Autocorrelation test identified 184 out of 1457 tested TFs as showing significant spatially-varying patterns of expression. We then compute cross-correlation metrics between these TFs, and run hierarchical clustering to idnetify modules with at-least 10 genes in each. Spot-level activity of each TF module is computed using the *calculate_module_scores* function and used for visualization in PC / tissue space.

Identifying Gene Expression Programs Associated With TF-Module Activity

We identified the top 1000 spots with highest score for each TF module, and compared the tumor-specific gene expression program in these spots as mentioned earlier, followed by gene ontology (GO) enrichment analysis. For module 9, we specifically contrasted it's expression profile against the top scoring cellular tumor (CT) and leading edge (LE) spots to identify unique molecular programs specifically enriched in this domain.

High Dimensional Weighted Gene Co-expression Analysis

High dimensional weighted gene co-expression network analysis (WGCNA) was performed on the Visium ST data using hdWGCNA v0.4.05 [13] in R. First, to address the sparsity inherent to Visium ST data, raw counts from spots passing QC were aggregated by spatial proximity into metaspots through summation of the counts in constituent spots (hdWGCNA::MetaspotsByGroup, layer = "counts", mode = "sum"). Aggregation grouping was defined such that metaspots only included spots from the same slide and IVY region. A minimum expression threshold was applied to metaspots, retaining genes with count > 1 in > 20% of samples. Metaspot counts were then normalized and log-transformed (hdWGCNA::NormalizeMetacells, normalization.method = "LogNormalize"). Outlying metaspots were removed using the standardized connectivity-based method implemented in the R package BioNERO v1.12.0 [224] with the standardized connectivity threshold set to -3 (BioNERO::ZKfiltering, zk = -3).

The resultant filtered and log-normalized expression data was then passed on to network construction. All network construction steps were performed using the biweight midcorrelation function and signed hybrid network type where applicable. The scale-free topology model fit for soft power thresholding values ranging from 4 to 16 was assessed (hdWGCNA::TestSoftPowers) and the lowest soft power achieving a fit of 0.80 was used for network construction. Co-expression network construction and module detection was performed using the ConstructNetwork function in hdWGCNA. This function first performs adjacency matrix construction, then topological overlap matrix construction from the gene expression data. The topological overlap matrix is used to cluster similar genes into an initial set of modules using the dynamic tree cut algorithm, with a minimum module size cutoff of 20 genes (minModuleSize = 20). This set of modules is then refined using partitioning around medoids-like gene-module reassignment (pamStage = TRUE, pamRespectsDendro = TRUE). Module eigengenes (MEs) were calculated and modules whose MEs were highly correlated were merged (mergeCutHeight = 0.15). Of note, ME calculation included correction for the slide of origin using the Harmony algorithm [225].

Hub genes were identified by ME-gene correlation (kME), where the larger gene set of either the top 10 or 10% of module genes were selected by kME. Enrichment of each module's gene set for pathways, ontologic terms, and drug targets was performed using the enrichR v3.4 package in R [226, 227, 228]. To focus on core module functionality, only up to the top 300 genes as sorted by kME were included in enrichment analysis for each module. The association between module expression levels and IVY region annotation was performed in two ways. First, for each region, one-vs-all testing was performed on MEs using the FindAllDMEs function in hdWGCNA, which performs wilcoxon rank-sum testing between MEs from spots in one

region against the MEs from spots in all other regions. Second, a linear mixed effect model was implemented using lmerTest v3.1-3 package in R [229]. In this approach, for each module, the ME was modeled against the one-hot-encoded IVY region assignment with a random intercept included for the slide.

Cell communication inference

To identify ligand-receptor pairs playing an active role in each Ivy GAP region, we developed a novel workflow integrating both SC and spatial analyses. We start by performing two analyses in parallel: identifying top interacting LR pairs using CellChat [100] from the GBMap single cell atlas with level 3 annotations, and identifying LR pairs whose spatial co-expression is significantly associated with the Ivy GAP region. To perform the first SC analysis, CellChat uses a mass action model to identify significantly interacting LR pairs between all possible cell type combinations. We performed global p-value adjustment using Benjamini-Hochberg (BH) to correct for false positives. To perform the second spatial analysis, we first calculated an LR co-expression metric over all 44 samples for those samples that had more than 1% of spots with non-zero ligand and receptor expression. For contact-based LR signaling, we simply calculated the product of ligand and receptor expression within the spot. For diffusion-based LR signaling, we calculated the spot-level bivariate Moran's statistic with a bandwidth of 1 radius away from the center spot. We then fit a mixed-effect model to represent the spatial co-expression scores as a function of the Ivy GAP region score using the sample as a random effect. We performed p-value adjustment through BH across all LR pairs for each region, selecting the pairs with significant and positive coefficient for that region. These pairs are interpreted to have increased co-expression deeper within the region of interest, ie, a likely higher interaction within this region.

We used commot [101] to create all spatial co-expression maps for validation. Commot uses optimal transport with the consideration that multiple ligands can bind to one receptor, and vice versa. While computationally inefficient for evaluating a large number of LR pairs, this method can identify both signaling strength and direction, while basic co-expression statistics (such as cosine similarity or bivariate moran's) cannot. This allows us to visualize strong localized signaling to validate region-specific CCI found by our quantitative workflow.

Association of LR pairs with network modules

To infer functional roles of top LR pairs per region, we integrated CCI with network analysis, modeling LR spatial co-expression as a function of module eigengene scores with sample as random effect. We performed p-value adjustment using BH across all modules for each LR pair, and ran this analysis for pairs unique to CT and MVP, as well as all pairs spatially associated with LE and PAN. The full results are shown in Figure S3, presenting all positive significant LR - module spatial associations ordered by the number of LR pairs with which a module is found associated. Through a literature review on the LR pairs associated with modules specific to the region, we can then hypothesize LR drivers of module mechanisms.

Direct association of LR pairs with functional pathways

An alternative method to discover downstream mechanisms activated by niche-specific LR pairs is direct gene association and enrichment. We modeled LR spatial co-expression as a function of differentially expressed genes taken over all regions, for top LR pairs per region. We performed p-value adjustment using BH across all genes per LR pair to identify those with a significant association. We then performed GO term pathway enrichment analysis on each set of significantly associated genes.

Data and Code Availability

The SC and ST data generated in this study are provided as Python AnnData objects through the following link (https://zenodo.org/records/16505469). Access to all code used in this analysis is available upon reasonable request.

Acknowledgements & Competing Interests

The authors do not have any competing interests or conflicts of interest related to this presented work. The work was supported by NINDS K08 NS128271, NCI P50-CA-269022, Chad Carr Pediatric Brain Tumor Center Research Award and grants from the B*Cured Foundation. Additionally, RK was funded by the Biomedical Informatics and Data Science Training Program (T32-GM141746).

References

1. Grochans, S. *et al.* Epidemiology of Glioblastoma Multiforme–Literature Review. *Cancers* **14**, 2412, DOI: 10.3390/cancers14102412 (2022).

2. Rodríguez-Camacho, A. *et al.* Glioblastoma Treatment: State-of-the-Art and Future Perspectives. *Int. J. Mol. Sci.* **23**, 7207, DOI: 10.3390/ijms23137207 (2022).

3. Shergalis, A., Bankhead, A., Luesakul, U., Muangsin, N. & Neamati, N. Current Challenges and Opportunities in Treating Glioblastomas. *Pharmacol. Rev.* **70**, 412–445, DOI: 10.1124/pr.117.014944 (2018). Publisher: Elsevier.

4. Puchalski, R. B. *et al.* An anatomic transcriptional atlas of human glioblastoma. *Science* **360**, 660–663 (2018).

5. Home :: Ivy Glioblastoma Atlas Project.

6. Liu, M. *et al.* Spatial transcriptomics reveals segregation of tumor cell states in glioblastoma and marked immunosuppression within the perinecrotic niche. *Acta Neuropathol. Commun.* **12**, 64 (2024).

7. Lv, X. *et al.* Decoding heterogeneous and coordinated tissue architecture in glioblastoma using spatial transcriptomics. *iScience* **27**, 110064, DOI: 10.1016/j.isci.2024.110064 (2024).

8. Ren, Y. *et al.* Spatial transcriptomics reveals niche-specific enrichment and vulnerabilities of radial glial stem-like cells in malignant gliomas. *Nat. Commun.* **14**, 1028, DOI: 10.1038/s41467-023-36707-6 (2023). Publisher: Nature Publishing Group.

9. Greenwald, A. C. *et al.* Integrative spatial analysis reveals a multi-layered organization of glioblastoma. *Cell* **187**, 2485–2501.e26, DOI: 10.1016/j.cell.2024.03.029 (2024). Publisher: Elsevier.

10. Feldman, L. Hypoxia within the glioblastoma tumor microenvironment: a master saboteur of novel treatments. *Front. Immunol.* **15**, 1384249 (2024).

11. Hara, T. *et al.* Interactions between cancer cells and immune cells drive transitions to mesenchymal-like states in glioblastoma. *Cancer cell* **39**, 779–792 (2021).

12. Ravi, V. M. *et al.* Spatially resolved multi-omics deciphers bidirectional tumor-host interdependence in glioblastoma. *Cancer cell* **40**, 639–655 (2022).

13. Morabito, S., Reese, F., Rahimzadeh, N., Miyoshi, E. & Swarup, V. hdWGCNA identifies co-expression networks in high-dimensional transcriptomics data. *Cell Reports Methods* **3**, DOI: 10.1016/j.crmeth.2023.100498 (2023). Publisher: Elsevier.

14. Ruiz-Moreno, C. *et al.* Harmonized single-cell landscape, intercellular crosstalk and tumor architecture of glioblastoma. *BioRxiv* 2022–08 (2022).

15. Andreatta, M. & Carmona, S. J. Ucell: Robust and scalable single-cell gene signature scoring. *Comput. structural biotechnology journal* **19**, 3796–3798 (2021).

16. Wei, R., Zhou, J., Bui, B. & Liu, X. Glioma actively orchestrate a self-advantageous extracellular matrix to promote recurrence and progression. *BMC cancer* **24**, 974 (2024).

17. Shimojo, H., Ohtsuka, T. & Kageyama, R. Oscillations in notch signaling regulate maintenance of neural progenitors. *Neuron* **58**, 52–64 (2008).

18. Bazzoni, R. & Bentivegna, A. Role of notch signaling pathway in glioblastoma pathogenesis. *Cancers* **11**, 292 (2019).

19. Sun, Y. *et al.* Brain-wide neuronal circuit connectome of human glioblastoma. *Nature* 1–3 (2025).

20. Iglesia, R. P. *et al.* Unconventional protein secretion in brain tumors biology: Enlightening the mechanisms for tumor survival and progression. *Front. cell developmental biology* **10**, 907423 (2022).

21. Cha, J. *et al.* Glioma cells secrete collagen vi to facilitate invasion. *bioRxiv* (2023).

22. Bastola, S. *et al.* Glioma-initiating cells at tumor edge gain signals from tumor core cells to promote their malignancy. *Nat. communications* **11**, 4660 (2020).

23. Rosberg, R. *et al.* Hypoxia-induced complement component 3 promotes aggressive tumor growth in the glioblastoma microenvironment. *JCI Insight* **9**, e179854, DOI: 10.1172/jci.insight.179854.

24. Tawil, N. *et al.* Glioblastoma cell populations with distinct oncogenic programs release podoplanin as procoagulant extracellular vesicles. *Blood advances* **5**, 1682–1694 (2021).

25. Yarmoska, S. K., Alawieh, A. M., Tomlinson, S. & Hoang, K. B. Modulation of the complement system by neoplastic disease of the central nervous system. *Front. Immunol.* **12**, 689435 (2021).

26. Zottel, A., Jovčevska, I., Šamec, N. & Komel, R. Cytoskeletal proteins as glioblastoma biomarkers and targets for therapy: A systematic review. *Critical reviews oncology/hematology* **160**, 103283 (2021).

27. Erasimus, H., Gobin, M., Niclou, S. & Van Dyck, E. Dna repair mechanisms and their clinical impact in glioblastoma. *Mutat. Res. Mutat. Res.* **769**, 19–35 (2016).

28. Begg, K. & Tavassoli, M. Inside the hypoxic tumour: reprogramming of the ddr and radioresistance. *Cell Death Discov.* **6**, 77 (2020).

29. Minata, M. *et al.* Phenotypic plasticity of invasive edge glioma stem-like cells in response to ionizing radiation. *Cell reports* **26**, 1893–1905 (2019).

30. Baxter, M. E., Miller, H. A., Chen, J., Williams, B. J. & Frieboes, H. B. Metabolomic differentiation of tumor core versus edge in glioma. *Neurosurg. Focus.* **54**, E4 (2023).

31. Kant, S. *et al.* Enhanced fatty acid oxidation provides glioblastoma cells metabolic plasticity to accommodate to its dynamic nutrient microenvironment. *Cell Death & Dis.* **11**, 253 (2020).

32. Garcia, J. H., Jain, S. & Aghi, M. K. Metabolic drivers of invasion in glioblastoma. *Front. cell developmental biology* **9**, 683276 (2021).

33. Hu, M. & Chikina, M. Instaprism: an r package for fast implementation of bayesprism. *Bioinformatics* **40**, btae440 (2024).

34. Seker-Polat, F., Pinarbasi Degirmenci, N., Solaroglu, I. & Bagci-Onder, T. Tumor cell infiltration into the brain in glioblastoma: from mechanisms to clinical perspectives. *Cancers* **14**, 443 (2022).

35. Larkin, C. J. *et al.* Myeloid cell classification and therapeutic opportunities within the glioblastoma tumor microenvironment in the single cell-omics era. *Front. immunology* **13**, 907605 (2022).

36. Pombo Antunes, A. R. *et al.* Understanding the glioblastoma immune microenvironment as basis for the development of new immunotherapeutic strategies. *elife* **9**, e52176 (2020).

37. Chen, Z. *et al.* Cellular and molecular identity of tumor-associated macrophages in glioblastoma. *Cancer research* **77**, 2266–2278 (2017).

38. Uribe, D. *et al.* Adapt to persist: Glioblastoma microenvironment and epigenetic regulation on cell plasticity. *Biology* **11**, 313 (2022).

39. Neftel, C. *et al.* An integrative model of cellular states, plasticity, and genetics for glioblastoma. *Cell* **178**, 835–849 (2019).

40. Nomura, M. *et al.* The multilayered transcriptional architecture of glioblastoma ecosystems. *Nat. Genet.* **57**, 697–710, DOI: 10.1038/s41588-025-02167-5 (2025).

41. Xiao, Y. *et al.* Single-cell transcriptomics revealed subtype-specific tumor immune microenvironments in human glioblastomas. *Front. immunology* **13**, 914236 (2022).

42. Chu, T., Wang, Z., Peâ€™er, D. & Danko, C. G. Cell type and gene expression deconvolution with bayesprism enables bayesian integrative analysis across bulk and single-cell rna sequencing in oncology. *Nat. cancer* **3**, 505–517 (2022).

43. Hu, M. & Chikina, M. Heterogeneous pseudobulk simulation enables realistic benchmarking of cell-type deconvolution methods. *Genome Biol.* **25**, 169 (2024).

44. Tran, K. A. *et al.* Performance of tumour microenvironment deconvolution methods in breast cancer using single-cell simulated bulk mixtures. *Nat. Commun.* **14**, 5758 (2023).

45. Richards, L. M. *et al.* Gradient of developmental and injury response transcriptional states defines functional vulnerabilities underpinning glioblastoma heterogeneity. *Nat. Cancer* **2**, 157–173 (2021).

46. Alfonso, J. Glioblastoma's widespread integration into neuronal networks. *Nat. Cancer* 1–1 (2025).

47. DeTomaso, D. & Yosef, N. Hotspot identifies informative gene modules across modalities of single-cell genomics. *Cell systems* **12**, 446–456 (2021).

48. Lambert, S. A. *et al.* The human transcription factors. *Cell* **172**, 650–665 (2018).

49. Marallano, V. J. *et al.* Hypoxia drives shared and distinct transcriptomic changes in two invasive glioma stem cell lines. *Sci. Reports* **14**, 7246 (2024).

50. Ngo, M. T., Sarkaria, J. N. & Harley, B. A. Perivascular stromal cells instruct glioblastoma invasion, proliferation, and therapeutic response within an engineered brain perivascular niche model. *Adv. Sci.* **9**, 2201888 (2022).

51. McCoy, M. G. *et al.* Endothelial cells promote 3d invasion of gbm by il-8-dependent induction of cancer stem cell properties. *Sci. reports* **9**, 9069 (2019).

52. Ben Mrid, R., El Guendouzi, S., Mineo, M. & El Fatimy, R. The emerging roles of aberrant alternative splicing in glioma. *Cell Death Discov.* **11**, 50 (2025).

53. Song, X. *et al.* Rna splicing analysis deciphers developmental hierarchies and reveals therapeutic targets in adult glioma. *The J. clinical investigation* **134** (2024).

54. Seidel, S. *et al.* A hypoxic niche regulates glioblastoma stem cells through hypoxia inducible factor 2α. *Brain* **133**, 983–995 (2010).

55. Stevanovic, M., Kovacevic-Grujicic, N., Mojsin, M., Milivojevic, M. & Drakulic, D. Sox transcription factors and glioma stem cells: Choosing between stemness and differentiation. *World journal stem cells* **13**, 1417 (2021).

56. Robertson, F. L. *et al.* Elevated foxg1 in glioblastoma stem cells cooperates with wnt/β-catenin to induce exit from quiescence. *Cell Reports* **42** (2023).

57. Yao, J. & Wang, L. Integrin α3 mediates stemness and invasion of glioblastoma by regulating pou3f2. *Curr. Protein Pept. Sci.* **24**, 247–256 (2023).

58. Kaur, B. *et al.* Hypoxia and the hypoxia-inducible-factor pathway in glioma growth and angiogenesis. *Neuro-Oncology* **7**, 134–153, DOI: 10.1215/S1152851704001060 (2005).

59. Wang, L. *et al.* The evolution of alternative splicing in glioblastoma under therapy. *Genome Biol.* **22**, 48, DOI: 10.1186/s13059-021-02259-5 (2021).

60. Katsushima, K. *et al.* Contribution of microRNA-1275 to Claudin11 protein suppression via a polycomb-mediated silencing mechanism in human glioma stem-like cells. *The J. Biol. Chem.* **287**, 27396–27406, DOI: 10.1074/jbc.M112.359109 (2012).

61. MOG myelin oligodendrocyte glycoprotein [Homo sapiens (human)] - Gene - NCBI.

62. myelin associated oligodendrocyte basic protein.

63. Yang, Y. *et al.* Four specific biomarkers associated with the progression of glioblastoma multiforme in older adults identified using weighted gene co-expression network analysis. *Bioengineered* **12**, 6643–6654, DOI: 10.1080/21655979.2021.1975980 (2021).

64. Hai, L. *et al.* Notch1 is a prognostic factor that is distinctly activated in the classical and proneural subtype of glioblastoma and that promotes glioma cell survival via the NF-B(p65) pathway. *Cell Death & Dis.* **9**, 158, DOI: 10.1038/s41419-017-0119-z (2018). Publisher: Nature Publishing Group.

65. Sun, Y. *et al.* Pan-cancer analysis reveals dual roles of HES6 in cancer immunity and prognosis. *Discov. Oncol.* **16**, 1110, DOI: 10.1007/s12672-025-02852-1 (2025).

66. González Alvarado, M. N. & Aprato, J. Sox8: a multifaceted transcription factor in development and disease. *Biol. Open* **14**, bio061840, DOI: 10.1242/bio.061840 (2025).

67. Chiu, C.-L., Zhao, H., Chen, C.-H., Wu, R. & Brooks, J. D. The Role of MARCKS in Metastasis and Treatment Resistance of Solid Tumors. *Cancers* **14**, 4925, DOI: 10.3390/cancers14194925 (2022).

68. Trépant, A.-L. *et al.* Identification of OLIG2 as the most specific glioblastoma stem cell marker starting from comparative analysis of data from similar DNA chip microarray platforms. *Tumour Biol. The J. Int. Soc. for Oncodevelopmental Biol. Medicine* **36**, 1943–1953, DOI: 10.1007/s13277-014-2800-5 (2015).

69. Barbosa, L. C., Machado, G. C., Heringer, M. & Ferrer, V. P. Identification of established and novel extracellular matrix components in glioblastoma as targets for angiogenesis and prognosis. *Neurogenetics* **25**, 249–262, DOI: 10.1007/s10048-024-00763-x (2024).

70. Nikitina, S. A. *et al.* The contribution of proteoglycans to heterogeneity and temozolomide resistance of glioblastoma cells. *J. Cancer Metastasis Treat.* **9**, N/A–N/A, DOI: 10.20517/2394-4722.2023.119 (2023). Publisher: OAE Publishing Inc.

71. Irshad, K. *et al.* A Combined Gene Signature of Hypoxia and Notch Pathway in Human Glioblastoma and Its Prognostic Relevance. *PLoS ONE* **10**, e0118201, DOI: 10.1371/journal.pone.0118201 (2015).

72. Kopanitsa, L., Kopanitsa, M. V., Safitri, D., Ladds, G. & Bailey, D. S. Suppression of Proliferation of Human Glioblastoma Cells by Combined Phosphodiesterase and Multidrug Resistance-Associated Protein 1 Inhibition. *Int. J. Mol. Sci.* **22**, 9665, DOI: 10.3390/ijms22189665 (2021).

73. Dixit, D. *et al.* Glioblastoma stem cells reprogram chromatin in vivo to generate selective therapeutic dependencies on DPY30 and phosphodiesterases. *Sci. Transl. Medicine* **14**, eabf3917, DOI: 10.1126/scitranslmed.abf3917 (2022). Publisher: American Association for the Advancement of Science.

74. Boukhari, A. *et al.* CD47 activation-induced UHRF1 over-expression is associated with silencing of tumor suppressor gene p16INK4A in glioblastoma cells. *Anticancer. Res.* **35**, 149–157 (2015).

75. Ma, R. *et al.* High expression of UBE2C is associated with the aggressive progression and poor outcome of malignant glioma. *Oncol. Lett.* **11**, 2300–2304, DOI: 10.3892/ol.2016.4171 (2016).

76. Wang, F. *et al.* Scutellarin inhibits the glioma cell proliferation by downregulating BIRC5 to promote cell apoptosis. *J. Cell. Mol. Medicine* **27**, 1975–1987, DOI: 10.1111/jcmm.17788 (2023).

77. Hu, Y. *et al.* Knockdown of NUSAP1 inhibits cell proliferation and invasion through downregulation of TOP2A in human glioblastoma. *Cell Cycle (Georgetown, Tex.)* **21**, 1842–1855, DOI: 10.1080/15384101.2022.2074199 (2022).

78. Li, C. *et al.* RRM2 promotes the progression of human glioblastoma. *J. Cell. Physiol.* **233**, 6759–6767, DOI: 10.1002/jcp.26529 (2018).

79. Zhao, M. *et al.* DHFR/TYMS are positive regulators of glioma cell growth and modulate chemo-sensitivity to temozolomide. *Eur. J. Pharmacol.* **863**, 172665, DOI: 10.1016/j.ejphar.2019.172665 (2019).

80. Su, X. *et al.* Inhibition of PTTG1 expression by microRNA suppresses proliferation and induces apoptosis of malignant glioma cells. *Oncol. Lett.* **12**, 3463–3471, DOI: 10.3892/ol.2016.5035 (2016).

81. Han, W. *et al.* HMGB2 is a biomarker associated with poor prognosis promoting radioresistance in glioma by targeting base excision repair pathway. *Transl. Oncol.* **45**, 101977, DOI: 10.1016/j.tranon.2024.101977 (2024).

82. TTYH3 tweety family member 3 [Homo sapiens (human)] - Gene - NCBI.

83. Wang, L., Ji, S., Liu, Z. & Zhao, J. Quercetin inhibits glioblastoma growth and prolongs survival rate through inhibiting glycolytic metabolism. *Chemotherapy* **67**, 132–141, DOI: 10.1159/000523905 (2022).

84. Ren, X. *et al.* Clusterin is a prognostic biomarker of lower-grade gliomas and is associated with immune cell infiltration. *Int. J. Mol. Sci.* **24**, 13413, DOI: 10.3390/ijms241713413 (2023).

85. Foster, E. M., Dangla-Valls, A., Lovestone, S., Ribe, E. M. & Buckley, N. J. Clusterin in alzheimer's disease: Mechanisms, genetics, and lessons from other pathologies. *Front. Neurosci.* **13**, 164, DOI: 10.3389/fnins.2019.00164 (2019).

86. Xu, Q. *et al.* Clusterin facilitates glioma progression via BCL2l1-dependent regulation of apoptotic resistance. *Front. Mol. Neurosci.* **18**, 1596021, DOI: 10.3389/fnmol.2025.1596021 (2025).

87. Breznik, B., Mitrović, A., Lah, T. T. & Kos, J. Cystatins in cancer progression: More than just cathepsin inhibitors. *Biochimie* **166**, 233–250, DOI: 10.1016/j.biochi.2019.05.002 (2019).

88. Schnittger, S., Rao, V., Abrahamson, M. & Hansmann, I. Cystatin c (CST3), the candidate gene for hereditary cystatin c amyloid angiopathy (HCCAA), and other members of the cystatin gene family are clustered on chromosome 20p11.2. *Genomics* **16**, 50–55, DOI: 10.1006/geno.1993.1139 (1993).

89. Wang, H. *et al.* S100B Promotes Glioma Growth through Chemoattraction of Myeloid-Derived Macrophages. *Clin. cancer research : an official journal Am. Assoc. for Cancer Res.* **19**, 3764–3775, DOI: 10.1158/1078-0432.CCR-12-3725 (2013).

90. Budnik, N. *et al.* The role of s-adenosylhomocysteine hydrolase-like 1 in cancer. *Biochimica et Biophys. Acta (BBA) - Mol. Cell Res.* **1871**, 119819, DOI: 10.1016/j.bbamcr.2024.119819 (2024).

91. Wang, B., Jiang, J., Luo, D. & Wang, X. Pan-cancer analysis reveals potential immunological and prognostic roles of METTL7a in human cancers. *Sci. Reports* **14**, 3476, DOI: 10.1038/s41598-024-54255-x (2024).

92. Mnatsakanyan, H. *et al.* CSIG-17. SCD5 PROTECTS GLIOBLASTOMA STEM CELLS FROM DEATH AND DIFFERENTIATION BY MODULATING INTRACELLULAR LIPID COMPOSITION. *Neuro-Oncology* **24**, vii42–vii42, DOI: 10.1093/neuonc/noac209.166 (2022).

93. Wen, J. *et al.* Clusterin-mediated polarization of m2 macrophages: a mechanism of temozolomide resistance in glioblastoma stem cells. *Stem Cell Res. & Ther.* **16**, 146, DOI: 10.1186/s13287-025-04247-z (2025).

94. Lattier, J. M. *et al.* Megalencephalic Leukoencephalopathy with Subcortical Cysts 1 (MLC1) Promotes Glioblastoma Cell Invasion in the Brain Microenvironment. *Oncogene* **39**, 7253–7264, DOI: 10.1038/s41388-020-01503-9 (2020).

95. Liu, Y. *et al.* Paradoxical role of 8 integrin on angiogenesis and vasculogenic mimicry in glioblastoma. *Cell Death & Dis.* **13**, 536, DOI: 10.1038/s41419-022-04959-7 (2022). Publisher: Nature Publishing Group.

96. Li, S. *et al.* Targeting 2 subunit of Na+/K+-ATPase induces glioblastoma cell apoptosis through elevation of intracellular Ca2+. *Am. J. Cancer Res.* **9**, 1293–1308 (2019).

97. Minchenko, D. O. *et al.* Hypoxic regulation of EDN1, EDNRA, EDNRB, and ECE1 gene expressions in ERN1 knockdown U87 glioma cells. *Endocr. Regul.* **53**, 250–262, DOI: 10.2478/enr-2019-0025 (2019).

98. Rashidi, A. *et al.* Myeloid cell-derived creatine in the hypoxic niche promotes glioblastoma growth. *Cell metabolism* **36**, 62–77.e8, DOI: 10.1016/j.cmet.2023.11.013 (2024).

99. Tseng, J.-H. *et al.* Valproic acid inhibits glioblastoma multiforme cell growth via paraoxonase 2 expression. *Oncotarget* **8**, 14666–14679, DOI: 10.18632/oncotarget.14716 (2017).

100. Jin, S. *et al.* Inference and analysis of cell-cell communication using cellchat. *Nat. Commun.* **12**, 1088, DOI: 10.1038/s41467-021-21246-9 (2021).

101. Cang, Z. *et al.* Screening cell–cell communication in spatial transcriptomics via collective optimal transport. *Nat. Methods* **20**, 218–228, DOI: 10.1038/s41592-022-01728-4 (2023). Publisher: Nature Publishing Group.

102. Saadeh, F. S., Mahfouz, R. & Assi, H. I. Egfr as a clinical marker in glioblastomas and other gliomas. *The Int. journal biological markers* **33**, 22–32 (2018).

103. Huang, P. H., Xu, A. M. & White, F. M. Oncogenic egfr signaling networks in glioma. *Sci. signaling* **2**, re6–re6 (2009).

104. Oprita, A. *et al.* Updated insights on egfr signaling pathways in glioma. *Int. journal molecular sciences* **22**, 587 (2021).

105. Chen, Y. *et al.* Tumor-associated monocytes promote mesenchymal transformation through egfr signaling in glioma. *Cell Reports Medicine* **4** (2023).

106. Aguirre, A., Dupree, J. L., Mangin, J. & Gallo, V. A functional role for egfr signaling in myelination and remyelination. *Nat. neuroscience* **10**, 990–1002 (2007).

107. Zaiss, D. M., Gause, W. C., Osborne, L. C. & Artis, D. Emerging functions of amphiregulin in orchestrating immunity, inflammation, and tissue repair. *Immunity* **42**, 216–226 (2015).

108. Sainio, A. & Järveläinen, H. Extracellular matrix-cell interactions: Focus on therapeutic applications. *Cell. signalling* **66**, 109487 (2020).

109. Cha, J. *et al.* Collagen vi deposition primes the glioblastoma microenvironment for invasion through mechanostimulation of β-catenin signaling. *PNAS nexus* **3**, pgae355 (2024).

110. Cescon, M. *et al.* Collagen vi sustains cell stemness and chemotherapy resistance in glioblastoma. *Cell. Mol. Life Sci.* **80**, 233 (2023).

111. Lathia, J. D. *et al.* Laminin alpha 2 enables glioblastoma stem cell growth. *Annals neurology* **72**, 766–778 (2012).

112. Yu, S. *et al.* GBP2 enhances glioblastoma invasion through Stat3/fibronectin pathway. *Oncogene* **39**, 5042–5055, DOI: 10.1038/s41388-020-1348-7 (2020). Publisher: Nature Publishing Group.

113. Long, H. *et al.* Prediction and Analysis of Key Genes in Glioblastoma Based on Bioinformatics. *BioMed Res. Int.* **2017**, 7653101, DOI: 10.1155/2017/7653101 (2017).

114. Yin, W. *et al.* Identification of collagen genes related to immune infiltration and epithelial-mesenchymal transition in glioma. *Cancer Cell Int.* **21**, 276, DOI: 10.1186/s12935-021-01982-0 (2021).

115. Chen, X. *et al.* Molecular mechanisms and therapeutic targets in glioblastoma multiforme: network and single-cell analyses. *Sci. Reports* **15**, 10558, DOI: 10.1038/s41598-025-92867-z (2025).

116. McGahan, B. G. *et al.* Assessment of Vascularity in Glioblastoma and Its Implications on Patient Outcomes. *J. neuro-oncology* **132**, 35–44, DOI: 10.1007/s11060-016-2350-3 (2017).

117. Li, X., Wang, N., Leng, H., Yuan, H. & Xu, L. Hsa_circ_0043949 reinforces temozolomide resistance via upregulating oncogene ITGA1 axis in glioblastoma. *Metab. Brain Dis.* **37**, 2979–2993, DOI: 10.1007/s11011-022-01069-3 (2022).

118. Li, Y. *et al.* Unveiling the role of TAGLN2 in glioblastoma: From proneural-mesenchymal transition to Temozolomide resistance. *Cancer Lett.* **598**, 217107, DOI: 10.1016/j.canlet.2024.217107 (2024).

119. Ulasov, I. V. *et al.* TMZ regulates GBM stemness via MMP14-DLL4-Notch3 pathway. *Int. J. Cancer* **146**, 2218–2228, DOI: 10.1002/ijc.32636 (2020). _eprint: https://onlinelibrary.wiley.com/doi/pdf/10.1002/ijc.32636.

120. Chen, P.-H. *et al.* The CHAC1-inhibited Notch3 pathway is involved in temozolomide-induced glioma cytotoxicity. *Neuropharmacology* **116**, 300–314, DOI: 10.1016/j.neuropharm.2016.12.011 (2017).

121. IM, M., ROH, J., JANG, W. & KIM, W. FN1 and VEGFA Are Potential Therapeutic Targets in Glioblastoma as Determined by Bioinformatics Analysis. *Cancer Genomics & Proteomics* **22**, 70–80, DOI: 10.21873/cgp.20488 (2025).

122. Han, Z. & Lu, Z.-R. Targeting Fibronectin for Cancer Imaging and Therapy. *J. materials chemistry. B, Mater. for biology medicine* **5**, 639–654, DOI: 10.1039/C6TB02008A (2017).

123. Xu, H. *et al.* Prognostic and predictive value of FCER1G in glioma outcomes and response to immunotherapy. *Cancer Cell Int.* **21**, 103, DOI: 10.1186/s12935-021-01804-3 (2021).

124. Kitange, G. J. *et al.* Expression of CD74 in high Grade Gliomas: A Potential Role in Temozolomide Resistance. *J. neuro-oncology* **100**, 177–186, DOI: 10.1007/s11060-010-0186-9 (2010).

125. Mangogna, A. *et al.* Prognostic Implications of the Complement Protein C1q in Gliomas. *Front. Immunol.* **10**, 2366, DOI: 10.3389/fimmu.2019.02366 (2019).

126. Zhu, H. *et al.* ROR1 facilitates glioblastoma growth via stabilizing GRB2 to promote c-Fos expression in glioma stem cells. *Neuro-Oncology* **27**, 695–710, DOI: 10.1093/neuonc/noae224 (2024).

127. Ramar, V. *et al.* Interaction of NF-B and FOSL1 drives glioma stemness. *Cell. Mol. Life Sci.* **81**, 255, DOI: 10.1007/s00018-024-05293-1 (2024).

128. Luo, D. *et al.* The PDK1/c-Jun pathway activated by TGF- induces EMT and promotes proliferation and invasion in human glioblastoma. *Int. J. Oncol.* **53**, 2067–2080, DOI: 10.3892/ijo.2018.4525 (2018). Publisher: Spandidos Publications.

129. Ueda, T., Kohama, Y. & Sakurai, H. IER family proteins are regulators of protein phosphatase PP2A and modulate the phosphorylation status of CDC25A. *Cell. Signal.* **55**, 81–89, DOI: 10.1016/j.cellsig.2018.12.012 (2019).

130. Murphy, C. *et al.* Modulation of Mcl-1 sensitizes glioblastoma to TRAIL-induced apoptosis. *Apoptosis* **19**, 629–642, DOI: 10.1007/s10495-013-0935-2 (2014).

131. Zhang, Y. *et al.* Mcl-1 downregulation sensitizes glioma to bortezomib-induced apoptosis. *Oncol. Reports* **33**, 2277–2284, DOI: 10.3892/or.2015.3875 (2015). Publisher: Spandidos Publications.

132. Lane, R. *et al.* PDGF-R inhibition induces glioblastoma cell differentiation via DUSP1/p38MAPK signalling. *Oncogene* **41**, 2749–2763, DOI: 10.1038/s41388-022-02294-x (2022).

133. Selmi, T. *et al.* ZFP36 expression impairs glioblastoma cell lines viability and invasiveness by targeting multiple signal transduction pathways. *Cell Cycle* **11**, 1977–1987, DOI: 10.4161/cc.20309 (2012). Publisher: Taylor & Francis _eprint: https://doi.org/10.4161/cc.20309.

134. Facchini, G. *et al.* Toxic effects of phytol and retinol on human glioblastoma cells are associated with modulation of cholesterol and fatty acid biosynthetic pathways. *J. Neuro-Oncology* **136**, 435–443, DOI: 10.1007/s11060-017-2672-9 (2018).

135. Moreb, J. S., Ucar-Bilyeu, D. A. & Khan, A. Use of retinoic acid/aldehyde dehydrogenase pathway as potential targeted therapy against cancer stem cells. *Cancer Chemother. Pharmacol.* **79**, 295–301, DOI: 10.1007/s00280-016-3213-5 (2017).

136. Tang, J. & Yang, R. All-Trans Retinoic Acid Induces Differentiation and Downregulates Stemness Markers and MGMT Expression in Glioblastoma Stem Cells. *Cells* **14**, 746, DOI: 10.3390/cells14100746 (2025).

137. Fu, M. *et al.* All-trans retinoic acid inhibits glioblastoma progression and attenuates radiation-induced brain injury. *JCI Insight* **9**, e179530, DOI: 10.1172/jci.insight.179530.

138. Alberts, B., Johnson, A., Lewis, J. *et al.* *Molecular Biology of the Cell* (Garland Science, New York, 2002), 4th edn. Available from: https://www.ncbi.nlm.nih.gov/books/NBK26867/.

139. Echavidre, W., Picco, V., Faraggi, M. & Montemagno, C. Integrin-αvβ3 as a therapeutic target in glioblastoma: back to the future? *Pharmaceutics* **14**, 1053 (2022).

140. Bae, E. *et al.* Integrin $\alpha3\beta1$ promotes vessel formation of glioblastoma-associated endothelial cells through calcium-mediated macropinocytosis and lysosomal exocytosis. *Nat. Commun.* **13**, 4268 (2022).

141. Paolillo, M., Serra, M. & Schinelli, S. Integrins in glioblastoma: Still an attractive target? *Pharmacol. Res.* **113**, 55–61 (2016).

142. Lieberman, J. Granzyme a activates another way to die. *Immunol. reviews* **235**, 93–104 (2010).

143. Gao, Y. *et al.* Heterogeneity induced gzma-f2r communication inefficient impairs antitumor immunotherapy of pd-1 mab through jak2/stat1 signal suppression in hepatocellular carcinoma. *Cell Death & Dis.* **13**, 213 (2022).

144. Kan, R. *et al.* Csig-15. ptn-ptprz1 signaling mediates tumor-normal crosstalk in glioblastoma. *Neuro-Oncology* **25**, v43 (2023).

145. Shi, Y. *et al.* Tumour-associated macrophages secrete pleiotrophin to promote ptprz1 signalling in glioblastoma stem cells for tumour growth. *Nat. communications* **8**, 15080 (2017).

146. Yang, M. *et al.* Ptn-ptprz1 signaling axis blocking mediates tumor microenvironment remodeling for enhanced glioblastoma treatment. *J. Control. Release* **353**, 63–76 (2023).

147. Mathur, R. *et al.* Glioblastoma evolution and heterogeneity from a 3d whole-tumor perspective. *Cell* **187**, 446–463 (2024).

148. Huang, W. *et al.* Origins and proliferative states of human oligodendrocyte precursor cells. *Cell* **182**, 594–608 (2020).

149. Knudsen, A. M. *et al.* Surgical resection of glioblastomas induces pleiotrophin-mediated self-renewal of glioblastoma stem cells in recurrent tumors. *Neuro-oncology* **24**, 1074–1087 (2022).

150. Tian, Y., Gao, X., Yang, X., Chen, S. & Ren, Y. VEGFA contributes to tumor property of glioblastoma cells by promoting differentiation of myeloid-derived suppressor cells. *BMC cancer* **24**, 1040, DOI: 10.1186/s12885-024-12803-8 (2024).

151. Liu, C. *et al.* Exploring the role of LOX family in glioma progression and immune modulation. *Front. Immunol.* **16**, 1512186, DOI: 10.3389/fimmu.2025.1512186 (2025).

152. Tsai, Y.-T. *et al.* ANGPTL4 Induces TMZ Resistance of Glioblastoma by Promoting Cancer Stemness Enrichment via the EGFR/AKT/4E-BP1 Cascade. *Int. J. Mol. Sci.* **20**, 5625, DOI: 10.3390/ijms20225625 (2019).

153. Yang, H. *et al.* The Role of NDRG1 Expression in Vasculogenic Mimicry of High-grade Gliomas. *J. Cancer* **15**, 6631–6643, DOI: 10.7150/jca.100458 (2024).

154. Hao, B. *et al.* Identification of SLC2A1 as a predictive biomarker for survival and response to immunotherapy in lung squamous cell carcinoma. *Comput. Biol. Medicine* **171**, 108183, DOI: 10.1016/j.compbiomed.2024.108183 (2024).

155. Ying, T., Lai, Y., Lu, S. & E, S. Identification and validation of a glycolysis-related taxonomy for improving outcomes in glioma. *CNS Neurosci. & Ther.* **30**, e14601, DOI: 10.1111/cns.14601 (2024).

156. Shakya, S. *et al.* Altered lipid metabolism marks glioblastoma stem and non-stem cells in separate tumor niches. *Acta Neuropathol. Commun.* **9**, 101, DOI: 10.1186/s40478-021-01205-7 (2021).

157. He, Z. *et al.* miR-1297 sensitizes glioma cells to temozolomide (TMZ) treatment through targeting adrenomedullin (ADM). *J. Transl. Medicine* **20**, 443, DOI: 10.1186/s12967-022-03647-6 (2022).

158. Wen, J. *et al.* Engineered nanovesicles targeting SERPINE1 overcome temozolomide resistance in glioblastoma. *Cell. Signal.* **132**, 111763, DOI: 10.1016/j.cellsig.2025.111763 (2025).

159. Zhao, K. *et al.* Inhibition of Carbonic Anhydrase 2 Overcomes Temozolomide Resistance in Glioblastoma Cells. *Int. J. Mol. Sci.* **23**, 157, DOI: 10.3390/ijms23010157 (2022). Number: 1 Publisher: Multidisciplinary Digital Publishing Institute.

160. Liang, Q. *et al.* Pan-cancer analysis of the prognosis and immunological role of AKAP12: A potential biomarker for resistance to anti-VEGF inhibitors. *Front. Genet.* **13**, 943006, DOI: 10.3389/fgene.2022.943006 (2022).

161. Ding, D., Lim, K. S. & Eberhart, C. G. Arsenic trioxide inhibits hedgehog, notch and stem cell properties in glioblastoma neurospheres. *Acta Neuropathol. Commun.* **2**, 31, DOI: 10.1186/2051-5960-2-31 (2014).

162. Bell, J. B. *et al.* Differential response of glioma stem cells to arsenic trioxide therapy is regulated by MNK1 and mRNA translation. *Mol. Cancer Res.* **16**, molcanres.0397.2017, DOI: 10.1158/1541-7786.mcr-17-0397 (2017).

163. Ma, K. *et al.* ANXA2 is correlated with the molecular features and clinical prognosis of glioma, and acts as a potential marker of immunosuppression. *Sci. Reports* **11**, 20839, DOI: 10.1038/s41598-021-00366-8 (2021).

164. Liu, L. *et al.* Sp1 induced gene TIMP1 is related to immune cell infiltration in glioblastoma. *Sci. Reports* **12**, 11181, DOI: 10.1038/s41598-022-14751-4 (2022).

165. Zhu, H. *et al.* TUBA1C is a Prognostic Marker in Low-grade Glioma and Correlates with Immune Cell Infiltration in the Tumor Microenvironment. *Front. Genet.* **12**, 759953, DOI: 10.3389/fgene.2021.759953 (2021).

166. Liu, T. *et al.* Potential role of TNFRSF12A in linking glioblastoma and alzheimer's disease via shared tumour suppressor pathways. *Sci. Reports* **15**, 21535, DOI: 10.1038/s41598-025-08000-7 (2025).

167. Chantaravisoot, N., Wongkongkathep, P., Loo, J. A., Mischel, P. S. & Tamanoi, F. Significance of filamin A in mTORC2 function in glioblastoma. *Mol. Cancer* **14**, 127, DOI: 10.1186/s12943-015-0396-z (2015).

168. Zottel, A. *et al.* Anti-Vimentin Nanobody Decreases Glioblastoma Cell Invasion In Vitro and In Vivo. *Cancers* **15**, 573, DOI: 10.3390/cancers15030573 (2023). Number: 3 Publisher: Multidisciplinary Digital Publishing Institute.

169. Han, S., Li, Z., Master, L. M., Master, Z. W. & Wu, A. Exogenous IGFBP-2 promotes proliferation, invasion, and chemoresistance to temozolomide in glioma cells via the integrin 1-ERK pathway. *Br. J. Cancer* **111**, 1400–1409, DOI: 10.1038/bjc.2014.435 (2014).

170. Zhou, P. *et al.* CD151-31 integrin complexes are prognostic markers of glioblastoma and cooperate with EGFR to drive tumor cell motility and invasion. *Oncotarget* **6**, 29675–29693, DOI: 10.18632/oncotarget.4896 (2015).

171. Liu, Y. *et al.* IGFBP2 promotes vasculogenic mimicry formation via regulating CD144 and MMP2 expression in glioma. *Oncogene* **38**, 1815–1831, DOI: 10.1038/s41388-018-0525-4 (2019). Publisher: Nature Publishing Group.

172. Aaberg-Jessen, C. *et al.* Co-expression of TIMP-1 and its cell surface binding partner CD63 in glioblastomas. *BMC Cancer* **18**, 270, DOI: 10.1186/s12885-018-4179-y (2018).

173. Schwartz, V. *et al.* A functional heteromeric mif receptor formed by cd74 and cxcr4. *FEBS letters* **583**, 2749–2757 (2009).

174. Ghoochani, A. *et al.* Mif-cd74 signaling impedes microglial m1 polarization and facilitates brain tumorigenesis. *Oncogene* **35**, 6246–6261 (2016).

175. Figueiredo, C. R. *et al.* Blockade of mif–cd74 signalling on macrophages and dendritic cells restores the antitumour immune response against metastatic melanoma. *Front. immunology* **9**, 1132 (2018).

176. Fukuda, Y. *et al.* Interplay between soluble cd74 and macrophage-migration inhibitory factor drives tumor growth and influences patient survival in melanoma. *Cell death & disease* **13**, 117 (2022).

177. Presti, M. *et al.* Overexpression of macrophage migration inhibitory factor and functionally-related genes, d-dt, cd74, cd44, cxcr2 and cxcr4, in glioblastoma. *Oncol. Lett.* **16**, 2881–2886 (2018).

178. Baron, N. *et al.* Role of macrophage migration inhibitory factor in primary glioblastoma multiforme cells. *J. neuroscience research* **89**, 711–717 (2011).

179. Guo, X. *et al.* Macrophage migration inhibitory factor promotes vasculogenic mimicry formation induced by hypoxia via cxcr4/akt/emt pathway in human glioblastoma cells. *Oncotarget* **8**, 1 7 4 0 9 – 1 7 4 2 0, DOI: 10.18632/oncotarget.18673 (2017). Published: June 27, 2017.

180. Puré, E. & Cuff, C. A. A crucial role for cd44 in inflammation. *Trends molecular medicine* **7**, 213–221 (2001).

181. Tang, W. *et al.* Revealing the role of spp1+ macrophages in glioma prognosis and therapeutic targeting by investigating tumor-associated macrophage landscape in grade 2 and 3 gliomas. *Cell & Biosci.* **14**, 37 (2024).

182. Trehan, R. *et al.* Spp1+ macrophages cause exhaustion of tumor-specific t cells in liver metastases. *Nat. Commun.* **16**, 4242 (2025).

183. Hou, L. *et al.* Targeting spp1+ macrophages via the spp1-cd44 axis reveals a key mechanism of immune suppression and tumor progression in ovarian cancer. *Int. Immunopharmacol.* **160**, 114906 (2025).

184. He, C. *et al.* Single-cell transcriptomic analysis revealed a critical role of spp1/cd44-mediated crosstalk between macrophages and cancer cells in glioma. *Front. Cell Dev. Biol.* **9**, 779319 (2021).

185. Huang, Q. *et al.* SNAP25 Inhibits Glioma Progression by Regulating Synapse Plasticity via GLS-Mediated Glutaminolysis. *Front. Oncol.* **11**, 698835, DOI: 10.3389/fonc.2021.698835 (2021).

186. Zou, S. *et al.* ATP1A3 Acts as a Potential Anti-oncogene in Glioblastoma via the Antagonizing Interaction with Small Nuclear Ribonucleoprotein Polypeptide G. *http://www.eurekaselect.com* (2025).

187. Barbagallo, D. *et al.* Dysregulated miR-671-5p / CDR1-AS / CDR1 / VSNL1 axis is involved in glioblastoma multiforme. *Oncotarget* **7**, 4746–4759, DOI: 10.18632/oncotarget.6621 (2015).

188. Fu, J. *et al.* Promoter Regulation of the Visinin-like Subfamily of Neuronal Calcium Sensor Proteins by Nuclear Respiratory Factor-1 *. *J. Biol. Chem.* **284**, 27577–27586, DOI: 10.1074/jbc.M109.049361 (2009). Publisher: Elsevier.

189. Lin, B. *et al.* Global analysis of H3K4me3 and H3K27me3 profiles in glioblastoma stem cells and identification of SLC17A7 as a bivalent tumor suppressor gene. *Oncotarget* **6**, 5369–5381, DOI: 10.18632/oncotarget.3030 (2015).

190. Yang, J., Yu, D., Liu, X., Changyong, E. & Yu, S. LINC00641/miR-4262/NRGN axis confines cell proliferation in glioma. *Cancer Biol. & Ther.* **21**, 758–766, DOI: 10.1080/15384047.2020.1776581.

191. Benarroch, E. What Is the Role of Stathmin-2 in Axonal Biology and Degeneration? *Neurology* **97**, 330–333, DOI: 10.1212/WNL.0000000000012419 (2021). Publisher: Wolters Kluwer.

192. Cao, Z., Zhu, J., Wang, Z., Peng, Y. & Zeng, L. Comprehensive pan-cancer analysis reveals ENC1 as a promising prognostic biomarker for tumor microenvironment and therapeutic responses. *Sci. Reports* **14**, 25331, DOI: 10.1038/s41598-024-76798-9 (2024). Publisher: Nature Publishing Group.

193. Feyissa, A. M., Rosenfeld, S. S. & Quiñones-Hinojosa, A. Altered glutamatergic and inflammatory pathways promote glioblastoma growth, invasion, and seizures: An overview. *J. Neurol. Sci.* **443**, DOI: 10.1016/j.jns.2022.120488 (2022). Publisher: Elsevier.

194. Srivastava, S. *et al.* Amino acid metabolism in glioblastoma pathogenesis, immune evasion, and treatment resistance. *Cancer Cell Int.* **25**, 89, DOI: 10.1186/s12935-025-03721-1 (2025).

195. Yates, J., Kraft, A. & Boeva, V. Filtering cells with high mitochondrial content depletes viable metabolically altered malignant cell populations in cancer single-cell studies. *Genome Biol.* **26**, 91, DOI: 10.1186/s13059-025-03559-w (2025).

196. Mei, P. Systematic analysis of the prognostic potential and functional roles of mitochondrially encoded protein coding genes in glioma. *Next Res.* **2**, 100350, DOI: 10.1016/j.nexres.2025.100350 (2025).

197. Yuan, X.-L., Wen, F.-Q., Chen, X.-W., Jiang, X.-P. & Liu, S.-X. miR-373 promotes neuroblastoma cell proliferation, migration, and invasion by targeting SRCIN1. *OncoTargets therapy* **12**, 4927–4936, DOI: 10.2147/OTT.S205582 (2019).

198. Dong, C. *et al.* PPFIBP1 induces glioma cell migration and invasion through FAK/Src/JNK signaling pathway. *Cell Death & Dis.* **12**, 827, DOI: 10.1038/s41419-021-04107-7 (2021). Publisher: Nature Publishing Group.

199. Xie, S. *et al.* TMEFF2 promoter hypermethylation is an unfavorable prognostic marker in gliomas. *Cancer Cell Int.* **21**, 148, DOI: 10.1186/s12935-021-01818-x (2021).

200. Tan, Y. *et al.* A comprehensive analysis of the prognostic and immunological role of ANK3 in pan-cancer. *Transl. Cancer Res.* **13**, 1091–1113, DOI: 10.21037/tcr-23-2379 (2024).

201. Greiner, M. *et al.* Silencing of the SEC62 gene inhibits migratory and invasive potential of various tumor cells. *Int. J. Cancer* **128**, 2284–2295, DOI: 10.1002/ijc.25580 (2011). _eprint: https://onlinelibrary.wiley.com/doi/pdf/10.1002/ijc.25580.

202. Yu, F. *et al.* SPOCK1 is upregulated in recurrent glioblastoma and contributes to metastasis and Temozolomide resistance. *Cell Prolif.* **49**, 195–206, DOI: 10.1111/cpr.12241 (2016).

203. Ren, J., Huang, P. & Wang, F. IGSF8 is a potential target for the treatment of gliomas. *Asian J. Surg.* **47**, 3883–3891, DOI: 10.1016/j.asjsur.2024.02.118 (2024).

204. MAP1B microtubule associated protein 1B [Homo sapiens (human)] - Gene - NCBI.

205. NTM neurotrimin [Homo sapiens (human)] - Gene - NCBI.

206. Rasila, T. *et al.* Astroprincin (FAM171A1, C10orf38): A Regulator of Human Cell Shape and Invasive Growth. *The Am. J. Pathol.* **189**, 177–189, DOI: 10.1016/j.ajpath.2018.09.006 (2019). Publisher: Elsevier.

207. Mazurek, M. *et al.* Metformin as potential therapy for high-grade glioma. *Cancers* **12**, 210, DOI: 10.3390/cancers12010210 (2020).

208. Shah, S., Mansour, H. M., Aguilar, T. M. & Lucke-Wold, B. Advances in anti-cancer drug development: Metformin as anti-angiogenic supplemental treatment for glioblastoma. *Int. J. Mol. Sci.* **25**, 5694, DOI: 10.3390/ijms25115694 (2024).

209. Mohammad, A. H. *et al.* Metformin use is associated with longer survival in glioblastoma patients with MGMT gene silencing. *J. Neuro-Oncology* **165**, 209–218, DOI: 10.1007/s11060-023-04485-2 (2023).

210. Mohebiany, A. N., Harroch, S. & Bouyain, S. New insights into the roles of the contactin cell adhesion molecules in neural development. *Cell Adhesion Mol. Implic. Neurol. Dis.* 165–194 (2013).

211. Zhu, B., Li, Y. & Mao, X. A review on the role of different ephrins in glioma. *Eur. J. Pharmacol.* **917**, 174588 (2022).

212. Nakada, M., Hayashi, Y. & Hamada, J.-i. Role of eph/ephrin tyrosine kinase in malignant glioma. *Neuro-Oncology* **13**, 1163–1170 (2011).

213. Day, B., Stringer, B. & Boyd, A. Eph receptors as therapeutic targets in glioblastoma. *Br. journal cancer* **111**, 1255–1261 (2014).

214. St. George-Hyslop, F., Kivisild, T. & Livesey, F. J. The role of contactin-associated protein-like 2 in neurodevelopmental disease and human cerebral cortex evolution. *Front. Mol. Neurosci.* **15**, 1017144 (2022).

215. Zhang, S. *et al.* Single-nucleus rna sequencing reveals cntnap2+ astrocytes triggering a hypertensive effect in the rostral ventrolateral medulla by disrupting glutamate uptake. *J. Adv. Res.* (2025). In press.

216. Zhang, J. *et al.* Glutamate affects cholesterol homeostasis within the brain via the up-regulation of cyp46a1 and apoe. *Toxicology* **432**, 152381, DOI: 10.1016/j.tox.2020.152381 (2020).

217. Brown, N. F., Carter, T. J., Ottaviani, D. & Mulholland, P. Harnessing the immune system in glioblastoma. *Br. J. Cancer* **119**, 1171–1181, DOI: 10.1038/s41416-018-0262-8 (2018).

218. Jain, S. *et al.* Single-cell rna sequencing and spatial transcriptomics reveal cancer-associated fibroblasts in glioblastoma with protumoral effects. *J. Clin. Investig.* **133**, e147087, DOI: 10.1172/JCI147087 (2023).

219. Hao, Y. *et al.* Dictionary learning for integrative, multimodal and scalable single-cell analysis. *Nat. Biotechnol.* **42**, 293–304, DOI: 10.1038/s41587-023-01767-y (2024). Publisher: Nature Publishing Group.

220. Dolgalev, I. msigdbr: MSigDB Gene Sets for Multiple Organisms in a Tidy Data Format (2025).

221. Xu, S. *et al.* Using clusterProfiler to characterize multiomics data. *Nat. Protoc.* **19**, 3292–3320, DOI: 10.1038/s41596-024-01020-z (2024). Publisher: Nature Publishing Group.

222. Yu, G. Thirteen years of clusterProfiler. *The Innov.* **5**, DOI: 10.1016/j.xinn.2024.100722 (2024). Publisher: Elsevier.

223. Friedman, J., Hastie, T. & Tibshirani, R. Sparse inverse covariance estimation with the graphical lasso. *Biostatistics* **9**, 432–441 (2008).

224. Almeida-Silva, F. & Venancio, T. M. BioNERO: an all-in-one R/Bioconductor package for comprehensive and easy biological network reconstruction. *Funct. & Integr. Genomics* **22**, 131–136, DOI: 10.1007/s10142-021-00821-9 (2022).

225. Korsunsky, I. *et al.* Fast, sensitive and accurate integration of single-cell data with Harmony. *Nat. Methods* **16**, 1289–1296, DOI: 10.1038/s41592-019-0619-0 (2019).

226. Xie, Z. *et al.* Gene Set Knowledge Discovery with Enrichr. *Curr. Protoc.* **1**, e90, DOI: 10.1002/cpz1.90 (2021). _eprint: https://currentprotocols.onlinelibrary.wiley.com/doi/pdf/10.1002/cpz1.90.

227. Kuleshov, M. V. *et al.* Enrichr: a comprehensive gene set enrichment analysis web server 2016 update. *Nucleic Acids Res.* **44**, W90–97, DOI: 10.1093/nar/gkw377 (2016).

228. Jawaid, W. enrichR: Provides an R Interface to 'Enrichr' (2025).

229. Kuznetsova, A., Brockhoff, P. B., Christensen, R. H. B. & Jensen, S. P. lmerTest: Tests in Linear Mixed Effects Models (2020).

Supporting information

S1 Fig. Supplementary to Figure 2. (A) Representative niche annotations for additional ST slides in our cohort. (B) Relative niche compositions of the 14 ST slides in our cohort. (C) Relative niche composition across all three study cohorts. (D) Spatial localization of EMT signature to MVP niche in slide 1512-A. (E) Cell-interaction graph across all 44 ST slides. Red lines indicate co-occurence, blue dotted lines indicate repulsion. (F) Localization of Ivy marker enrichment scores to distinct portions of 2D PCA embedding indicates the embedding captures continuous spatial gradients between niches.

S2 Fig. Supplementary to Figure 3. (A) Spatial activity of TF modules identified with Hotspot analysis. (B) Specific transcription factors that are in Module-9 and their local correlaiton scores. (C) Mean activity of TF modules by slide shows importance of having a large cohort to identify distinct spatially localized programs in the disease due to bias in sampling areas.

S3 Fig. All LR-pair module associations. All positive associations between regional LR pairs and gene coexpression network modules.

S4 Fig. Direct regional LR-pathway analysis. Pathway enrichment of genes significantly associated with regional LR pairs.

S5 Fig. CellChat results for non-tumor state interactions enriched in MVP.

S6 Table Gene coexpression network module genes.

S7 Table Gene coexpression module enrichment results.

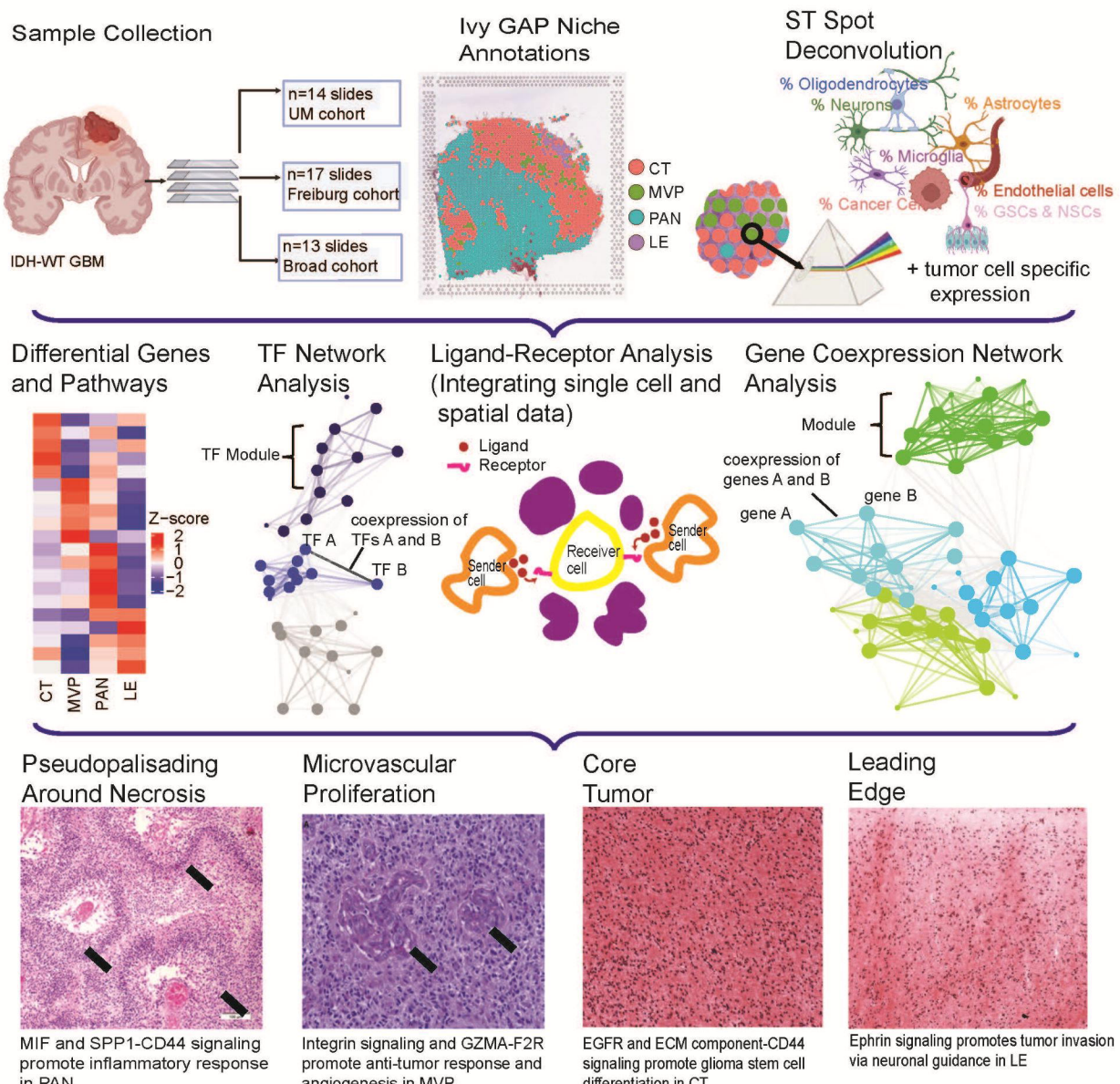
Sample Collection
IDH-WT GBM
n=14 slides
UM cohort
n=17 slides
Freiburg cohort
n=13 slides
Broad cohort
Ivy GAP Niche Annotations
CT
MVP
PAN
LE
ST Spot Deconvolution
% Oligodendrocytes
% Neurons
% Astrocytes
% Microglia
% Cancer Cells
% Endothelial cells
% GSCs & NSCs
+ tumor cell specific expression
Differential Genes and Pathways
Z-score
2
1
0
−1
−2
CT
MVP
PAN
LE
TF Network Analysis
TF Module
coexpression of TFs A and B
TF A
TF B
Ligand-Receptor Analysis (Integrating single cell and spatial data)
Ligand
Receptor
Sender cell
Receiver cell
Sender cell
Gene Coexpression Network Analysis
Module
coexpression of genes A and B
gene A
gene B
Pseudopalisading Around Necrosis
MIF and SPP1-CD44 signaling promote inflammatory response in PAN
Microvascular Proliferation
Integrin signaling and GZMA-F2R promote anti-tumor response and angiogenesis in MVP
Core Tumor
EGFR and ECM component-CD44 signaling promote glioma stem cell differentiation in CT
Leading Edge
Ephrin signaling promotes tumor invasion via neuronal guidance in LE

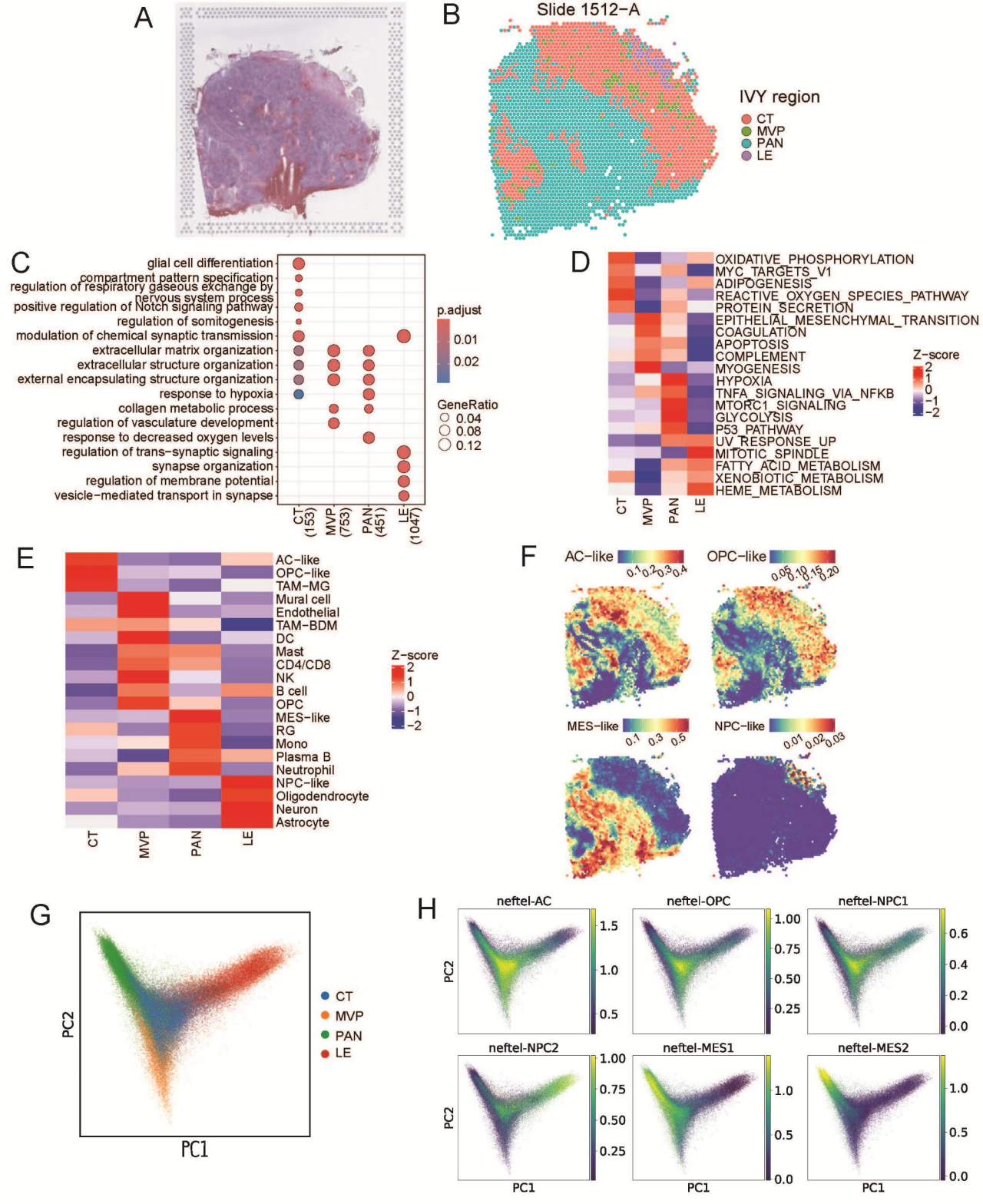
A
B
Slide 1512−A
IVY region
CT
MVP
PAN
LE
C
glial cell differentiation
compartment pattern specification
regulation of respiratory gaseous exchange by nervous system process
positive regulation of Notch signaling pathway
regulation of somitogenesis
modulation of chemical synaptic transmission
extracellular matrix organization
extracellular structure organization
external encapsulating structure organization
response to hypoxia
collagen metabolic process
regulation of vasculature development
response to decreased oxygen levels
regulation of trans−synaptic signaling
synapse organization
regulation of membrane potential
vesicle−mediated transport in synapse
CT (153)
MVP (753)
PAN (451)
LE (1047)
p.adjust
0.01
0.02
GeneRatio
0.04
0.08
0.12
D
OXIDATIVE_PHOSPHORYLATION
MYC_TARGETS_V1
ADIPOGENESIS
REACTIVE_OXYGEN_SPECIES_PATHWAY
PROTEIN_SECRETION
EPITHELIAL_MESENCHYMAL_TRANSITION
COAGULATION
APOPTOSIS
COMPLEMENT
MYOGENESIS
HYPOXIA
TNFA_SIGNALING_VIA_NFKB
MTORC1_SIGNALING
GLYCOLYSIS
P53_PATHWAY
UV_RESPONSE_UP
MITOTIC_SPINDLE
FATTY_ACID_METABOLISM
XENOBIOTIC_METABOLISM
HEME_METABOLISM
CT
MVP
PAN
LE
Z−score
2
1
0
−1
−2
E
AC−like
OPC−like
TAM−MG
Mural cell
Endothelial
TAM−BDM
DC
Mast
CD4/CD8
NK
B cell
OPC
MES−like
RG
Mono
Plasma B
Neutrophil
NPC−like
Oligodendrocyte
Neuron
Astrocyte
CT
MVP
PAN
LE
Z−score
2
1
0
−1
−2
F
AC−like
0.1 0.2 0.3 0.4
OPC−like
0.05 0.10 0.15 0.20
MES−like
0.1 0.3 0.5
NPC−like
0.01 0.02 0.03
G
PC2
PC1
CT
MVP
PAN
LE
H
neftel−AC
neftel−OPC
neftel−NPC1
neftel−NPC2
neftel−MES1
neftel−MES2
PC2
PC1
1.5
1.0
0.5
1.00
0.75
0.50
0.25
0.6
0.4
0.2
0.0

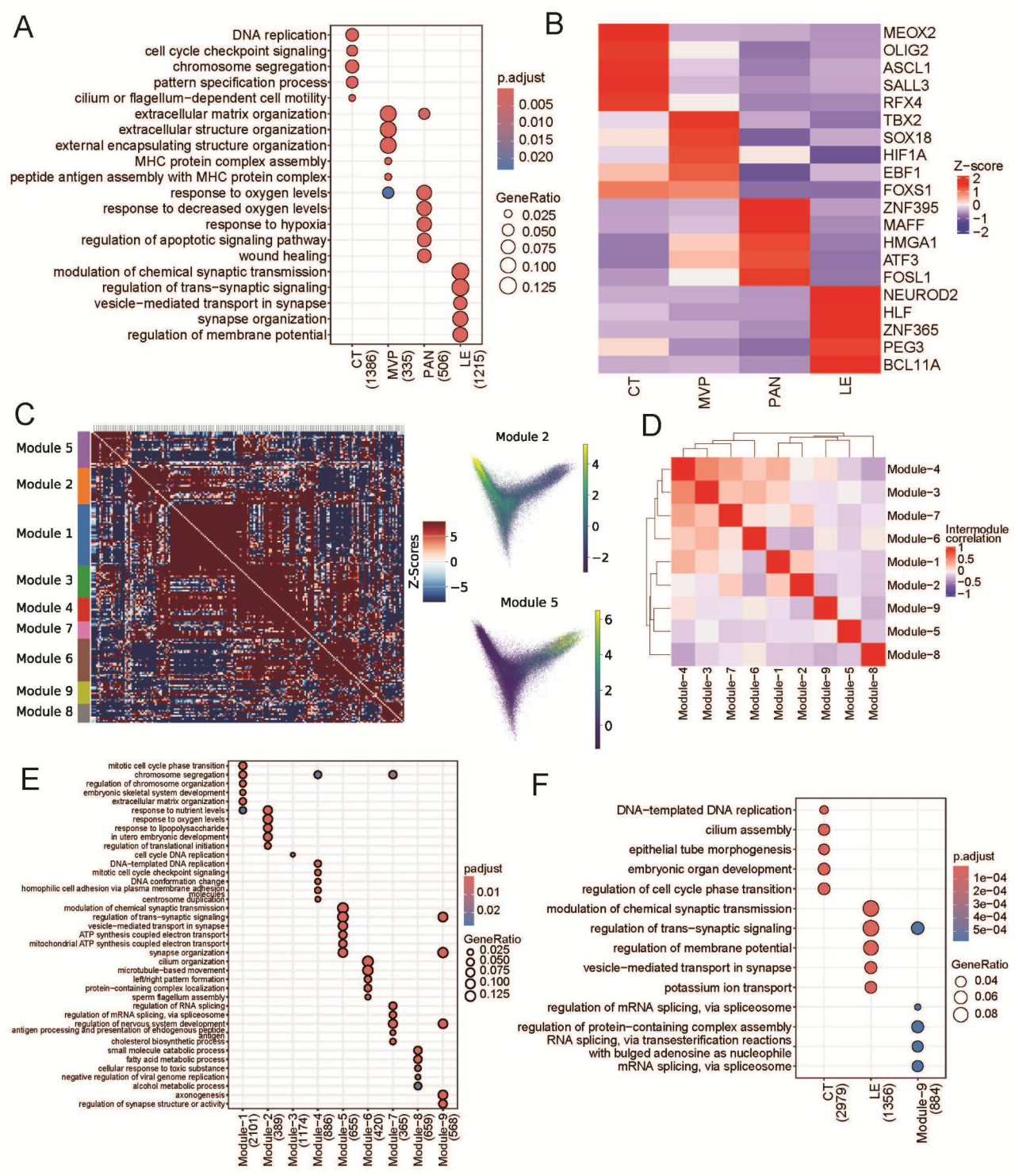
A
DNA replication
cell cycle checkpoint signaling
chromosome segregation
pattern specification process
cilium or flagellum-dependent cell motility
extracellular matrix organization
extracellular structure organization
external encapsulating structure organization
MHC protein complex assembly
peptide antigen assembly with MHC protein complex
response to oxygen levels
response to decreased oxygen levels
response to hypoxia
regulation of apoptotic signaling pathway
wound healing
modulation of chemical synaptic transmission
regulation of trans-synaptic signaling
vesicle-mediated transport in synapse
synapse organization
regulation of membrane potential
CT (1386)
MVP (335)
PAN (506)
LE (1215)
p.adjust
0.005
0.010
0.015
0.020
GeneRatio
0.025
0.050
0.075
0.100
0.125
B
MEOX2
OLIG2
ASCL1
SALL3
RFX4
TBX2
SOX18
HIF1A
EBF1
FOXS1
ZNF395
MAFF
HMGA1
ATF3
FOSL1
NEUROD2
HLF
ZNF365
PEG3
BCL11A
CT
MVP
PAN
LE
Z-score
2
1
0
−1
−2
C
Module 5
Module 2
Module 1
Module 3
Module 4
Module 7
Module 6
Module 9
Module 8
Z-Scores
5
0
−5
Module 2
4
2
0
−2
Module 5
6
4
2
0
D
Module-4
Module-3
Module-7
Module-6
Module-1
Module-2
Module-9
Module-5
Module-8
Intermodule correlation
1
0.5
0
−0.5
−1
E
mitotic cell cycle phase transition
chromosome segregation
regulation of chromosome organization
embryonic skeletal system development
extracellular matrix organization
response to nutrient levels
response to oxygen levels
response to lipopolysaccharide
in utero embryonic development
regulation of translational initiation
cell cycle DNA replication
DNA-templated DNA replication
mitotic cell cycle checkpoint signaling
DNA conformation change
homophilic cell adhesion via plasma membrane adhesion molecules
centrosome duplication
modulation of chemical synaptic transmission
regulation of trans-synaptic signaling
vesicle-mediated transport in synapse
ATP synthesis coupled electron transport
mitochondrial ATP synthesis coupled electron transport
synapse organization
cilium organization
microtubule-based movement
left/right pattern formation
protein-containing complex localization
sperm flagellum assembly
regulation of RNA splicing
regulation of mRNA splicing, via spliceosome
regulation of nervous system development
antigen processing and presentation of endogenous peptide antigen
cholesterol biosynthetic process
small molecule catabolic process
fatty acid metabolic process
cellular response to toxic substance
negative regulation of viral genome replication
alcohol metabolic process
axonogenesis
regulation of synapse structure or activity
Module-1 (2101)
Module-2 (389)
Module-3 (1174)
Module-4 (886)
Module-5 (655)
Module-6 (420)
Module-7 (365)
Module-8 (659)
Module-9 (568)
padjust
0.01
0.02
GeneRatio
0.025
0.050
0.075
0.100
0.125
F
DNA-templated DNA replication
cilium assembly
epithelial tube morphogenesis
embryonic organ development
regulation of cell cycle phase transition
modulation of chemical synaptic transmission
regulation of trans-synaptic signaling
regulation of membrane potential
vesicle-mediated transport in synapse
potassium ion transport
regulation of mRNA splicing, via spliceosome
regulation of protein-containing complex assembly
RNA splicing, via transesterification reactions with bulged adenosine as nucleophile
mRNA splicing, via spliceosome
CT (2979)
LE (1356)
Module-9 (884)
p.adjust
1e-04
2e-04
3e-04
4e-04
5e-04
GeneRatio
0.04
0.06
0.08

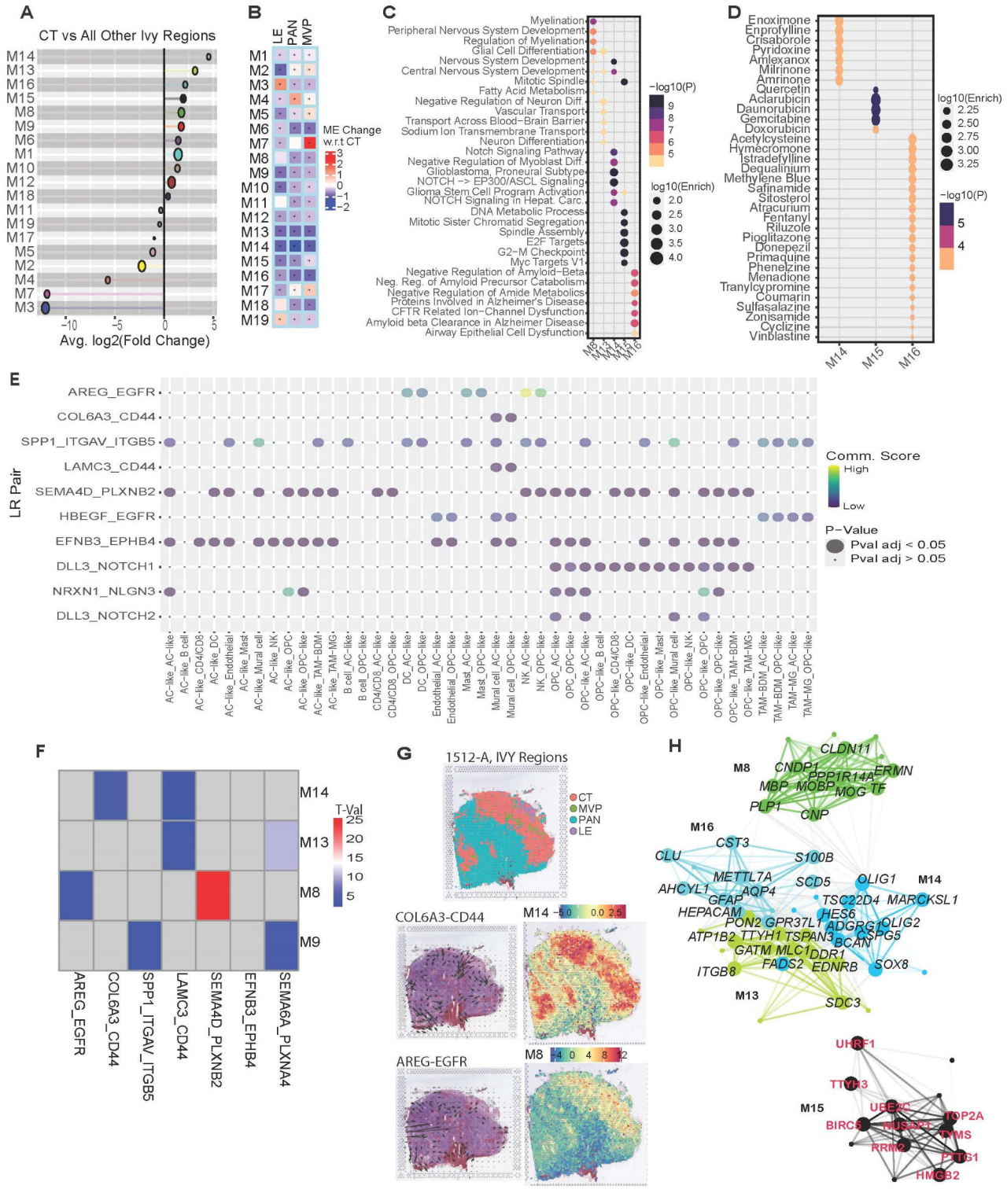
A
CT vs All Other Ivy Regions
M14
M13
M16
M15
M8
M9
M6
M1
M10
M12
M18
M11
M19
M17
M5
M2
M4
M7
M3
-10
-5
0
5
Avg. log2(Fold Change)
B
LE
PAN
MVP
M1
M2
M3
M4
M5
M6
M7
M8
M9
M10
M11
M12
M13
M14
M15
M16
M17
M18
M19
ME Change w.r.t CT
3
2
1
0
−1
−2
C
Myelination
Peripheral Nervous System Development
Regulation of Myelination
Glial Cell Differentiation
Nervous System Development
Central Nervous System Development
Mitotic Spindle
Fatty Acid Metabolism
Negative Regulation of Neuron Diff.
Vascular Transport
Transport Across Blood−Brain Barrier
Sodium Ion Transmembrane Transport
Neuron Differentiation
Notch Signaling Pathway
Negative Regulation of Myoblast Diff.
Glioblastoma, Proneural Subtype
NOTCH −> EP300/ASCL Signaling
Glioma Stem Cell Program Activation
NOTCH Signaling in Hepat. Carc.
DNA Metabolic Process
Mitotic Sister Chromatid Segregation
Spindle Assembly
E2F Targets
G2−M Checkpoint
Myc Targets V1
Negative Regulation of Amyloid−Beta
Neg. Reg. of Amyloid Precursor Catabolism
Negative Regulation of Amide Metabolics
Proteins Involved in Alzheimer's Disease
CFTR Related Ion−Channel Dysfunction
Amyloid beta Clearance in Alzheimer Disease
Airway Epithelial Cell Dysfunction
M8
M13
M14
M15
M16
−log10(P)
9
8
7
6
5
log10(Enrich)
2.0
2.5
3.0
3.5
4.0
D
Enoximone
Enprofylline
Crisaborole
Pyridoxine
Amlexanox
Milrinone
Amrinone
Quercetin
Aclarubicin
Daunorubicin
Gemcitabine
Doxorubicin
Acetylcysteine
Hymecromone
Istradefylline
Dequalinium
Methylene Blue
Safinamide
Sitosterol
Atracurium
Fentanyl
Riluzole
Pioglitazone
Donepezil
Primaquine
Phenelzine
Menadione
Tranylcypromine
Coumarin
Sulfasalazine
Zonisamide
Cyclizine
Vinblastine
M14
M15
M16
log10(Enrich)
2.25
2.50
2.75
3.00
3.25
−log10(P)
5
4
E
LR Pair
AREG_EGFR
COL6A3_CD44
SPP1_ITGAV_ITGB5
LAMC3_CD44
SEMA4D_PLXNB2
HBEGF_EGFR
EFNB3_EPHB4
DLL3_NOTCH1
NRXN1_NLGN3
DLL3_NOTCH2
AC−like_AC−like
AC−like_B cell
AC−like_CD4/CD8
AC−like_DC
AC−like_Endothelial
AC−like_Mast
AC−like_Mural cell
AC−like_NK
AC−like_OPC
AC−like_OPC−like
AC−like_TAM−BDM
AC−like_TAM−MG
B cell_AC−like
B cell_OPC−like
CD4/CD8_AC−like
CD4/CD8_OPC−like
DC_AC−like
DC_OPC−like
Endothelial_AC−like
Endothelial_OPC−like
Mast_AC−like
Mast_OPC−like
Mural cell_AC−like
Mural cell_OPC−like
NK_AC−like
NK_OPC−like
OPC_AC−like
OPC_OPC−like
OPC−like_AC−like
OPC−like_B cell
OPC−like_CD4/CD8
OPC−like_DC
OPC−like_Endothelial
OPC−like_Mast
OPC−like_Mural cell
OPC−like_NK
OPC−like_OPC
OPC−like_OPC−like
OPC−like_TAM−BDM
OPC−like_TAM−MG
TAM−BDM_AC−like
TAM−BDM_OPC−like
TAM−MG_AC−like
TAM−MG_OPC−like
Comm. Score
High
Low
P−Value
Pval adj < 0.05
Pval adj > 0.05
F
M14
M13
M8
M9
T-Val
25
20
15
10
5
AREG_EGFR
COL6A3_CD44
SPP1_ITGAV_ITGB5
LAMC3_CD44
SEMA4D_PLXNB2
EFNB3_EPHB4
SEMA6A_PLXNA4
G
1512-A, IVY Regions
CT
MVP
PAN
LE
COL6A3-CD44
M14
-5.0
0.0
2.5
AREG-EGFR
M8
-4
0
4
8
12
H
M8
CLDN11
CNDP1
ERMN
PPP1R14A
MBP
MOBP
MOG
TF
PLP1
CNP
M16
CST3
CLU
S100B
METTL7A
SCD5
OLIG1
M14
AHCYL1
AQP4
GFAP
TSC22D4
MARCKSL1
HEPACAM
HES6
PON2
GPR37L1
ADGRG1
OLIG2
ATP1B2
TTYH1
TSPAN3
CSPG5
BCAN
GATM
MLC1
DDR1
FADS2
EDNRB
SOX8
ITGB8
M13
SDC3
M15
UHRF1
TTYH3
UBE2C
TOP2A
BIRC5
HUSAP1
TYMS
RRM2
FTCD
HMGB2

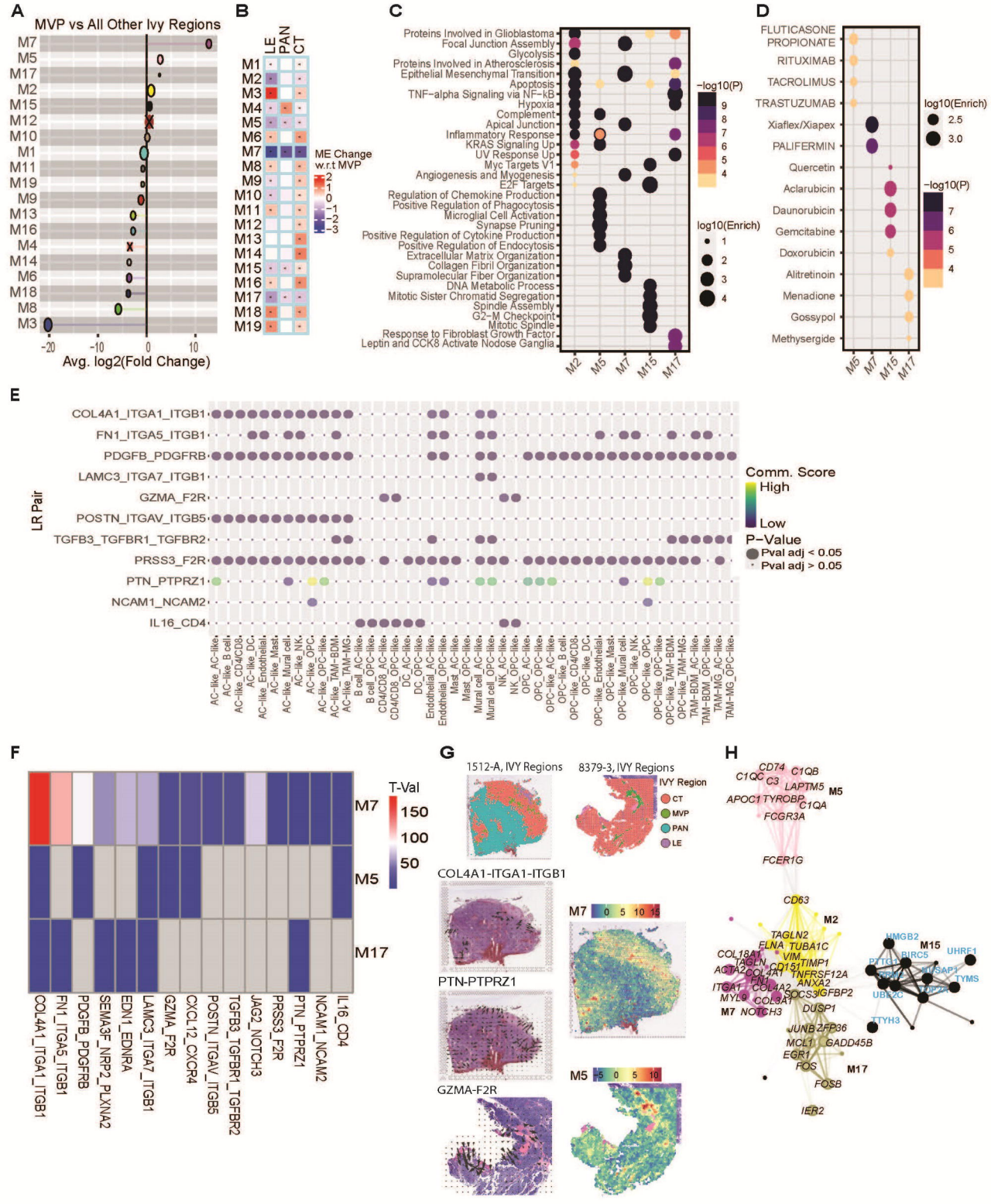
A
MVP vs All Other Ivy Regions
M7
M5
M17
M2
M15
M12
M10
M1
M11
M19
M9
M13
M16
M4
M14
M6
M18
M8
M3
-20
-10
0
10
Avg. log2(Fold Change)
B
LE
PAN
CT
M1
M2
M3
M4
M5
M6
M7
M8
M9
M10
M11
M12
M13
M14
M15
M16
M17
M18
M19
ME Change w.r.t MVP
2
1
0
−1
−2
−3
C
Proteins Involved in Glioblastoma
Focal Junction Assembly
Glycolysis
Proteins Involved in Atherosclerosis
Epithelial Mesenchymal Transition
Apoptosis
TNF−alpha Signaling via NF−kB
Hypoxia
Complement
Apical Junction
Inflammatory Response
KRAS Signaling Up
UV Response Up
Myc Targets V1
Angiogenesis and Myogenesis
E2F Targets
Regulation of Chemokine Production
Positive Regulation of Phagocytosis
Microglial Cell Activation
Synapse Pruning
Positive Regulation of Cytokine Production
Positive Regulation of Endocytosis
Extracellular Matrix Organization
Collagen Fibril Organization
Supramolecular Fiber Organization
DNA Metabolic Process
Mitotic Sister Chromatid Segregation
Spindle Assembly
G2−M Checkpoint
Mitotic Spindle
Response to Fibroblast Growth Factor
Leptin and CCK8 Activate Nodose Ganglia
M2
M5
M7
M15
M17
−log10(P)
9
8
7
6
5
4
log10(Enrich)
1
2
3
4
D
FLUTICASONE PROPIONATE
RITUXIMAB
TACROLIMUS
TRASTUZUMAB
Xiaflex/Xiapex
PALIFERMIN
Quercetin
Aclarubicin
Daunorubicin
Gemcitabine
Doxorubicin
Alitretinoin
Menadione
Gossypol
Methysergide
M5
M7
M15
M17
log10(Enrich)
2.5
3.0
−log10(P)
7
6
5
4
E
LR Pair
COL4A1_ITGA1_ITGB1
FN1_ITGA5_ITGB1
PDGFB_PDGFRB
LAMC3_ITGA7_ITGB1
GZMA_F2R
POSTN_ITGAV_ITGB5
TGFB3_TGFBR1_TGFBR2
PRSS3_F2R
PTN_PTPRZ1
NCAM1_NCAM2
IL16_CD4
AC−like_AC−like
AC−like_B cell
AC−like_CD4/CD8
AC−like_DC
AC−like_Endothelial
AC−like_Mast
AC−like_Mural cell
AC−like_NK
AC−like_OPC
AC−like_OPC−like
AC−like_TAM−BDM
AC−like_TAM−MG
B cell_AC−like
B cell_OPC−like
CD4/CD8_AC−like
CD4/CD8_OPC−like
DC_AC−like
DC_OPC−like
Endothelial_AC−like
Endothelial_OPC−like
Mast_AC−like
Mast_OPC−like
Mural cell_AC−like
Mural cell_OPC−like
NK_AC−like
NK_OPC−like
OPC_AC−like
OPC_OPC−like
OPC−like_AC−like
OPC−like_B cell
OPC−like_CD4/CD8
OPC−like_DC
OPC−like_Endothelial
OPC−like_Mast
OPC−like_Mural cell
OPC−like_NK
OPC−like_OPC
OPC−like_OPC−like
OPC−like_TAM−BDM
OPC−like_TAM−MG
TAM−BDM_AC−like
TAM−BDM_OPC−like
TAM−MG_AC−like
TAM−MG_OPC−like
Comm. Score
High
Low
P−Value
Pval adj < 0.05
Pval adj > 0.05
F
T-Val
150
100
50
M7
M5
M17
COL4A1_ITGA1_ITGB1
FN1_ITGA5_ITGB1
PDGFB_PDGFRB
SEMA3F_NRP2_PLXNA2
EDN1_EDNRA
LAMC3_ITGA7_ITGB1
GZMA_F2R
CXCL12_CXCR4
POSTN_ITGAV_ITGB5
TGFB3_TGFBR1_TGFBR2
JAG2_NOTCH3
PRSS3_F2R
PTN_PTPRZ1
NCAM1_NCAM2
IL16_CD4
G
1512-A, IVY Regions
8379-3, IVY Regions
IVY Region
CT
MVP
PAN
LE
COL4A1-ITGA1-ITGB1
PTN-PTPRZ1
GZMA-F2R
M7
0
5
10
15
M5
-5
0
5
10
H
CD74
C1QC
C1QB
C3
LAPTM5
M5
APOC1
TYROBP
C1QA
FCGR3A
FCER1G
CD63
M2
TAGLN2
FLNA
TUBA1C
COL18A1
VIM
TAGLN
CD151
TIMP1
ACTA2
COL4A1
TNFRSF12A
FN1
ANXA2
ITGA1
COL4A2
SOCS3
IGFBP2
MYL9
COL3A1
M7
NOTCH3
DUSP1
JUNB
ZFP36
MCL1
GADD45B
EGR1
FOS
M17
FOSB
IER2
UMGB2
M15
BIRC5
UHRF1
PTTG1
NUSAP1
TYMS
UBE2C
TOP2A
TTYH3

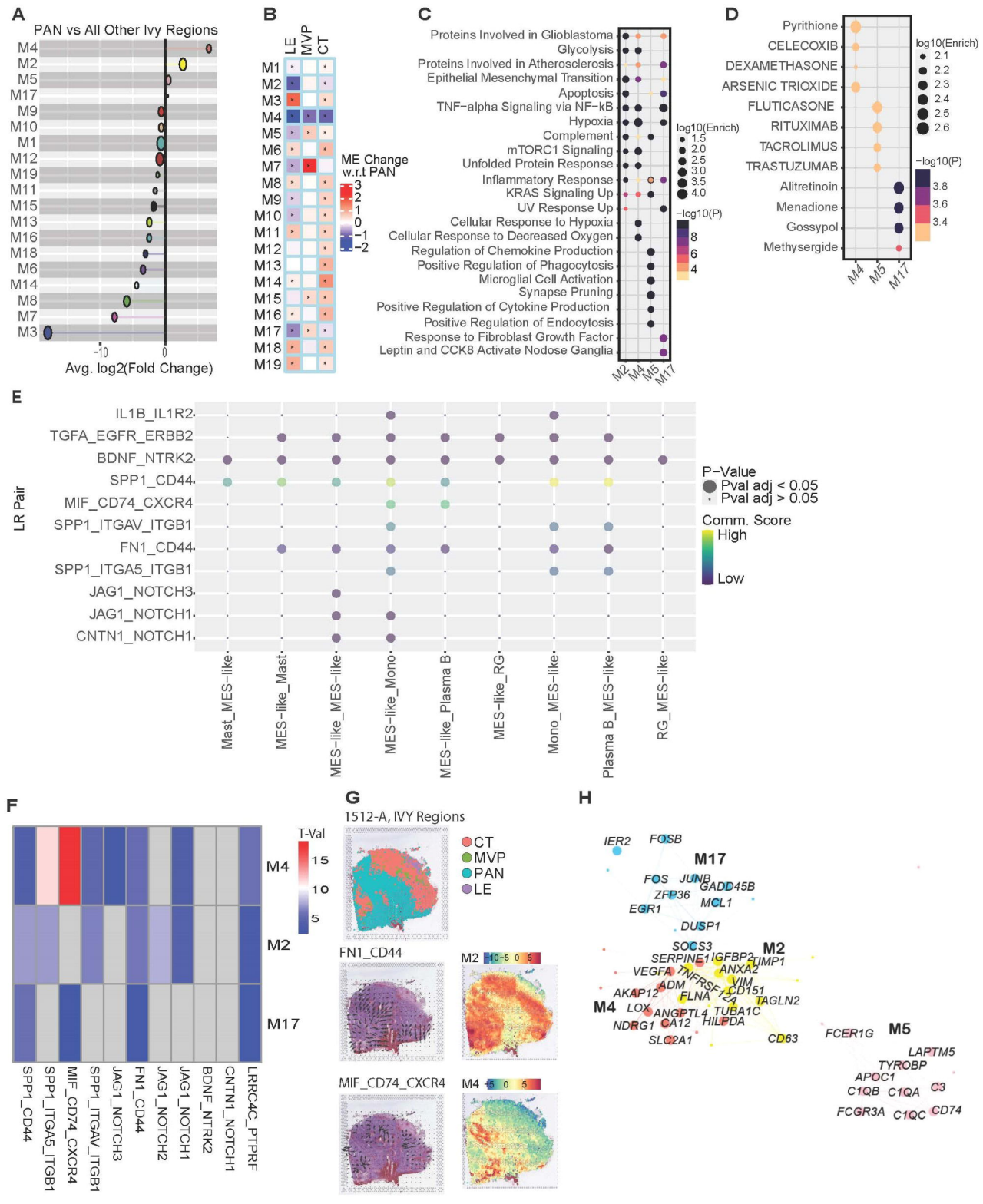
A
PAN vs All Other Ivy Regions
M4
M2
M5
M17
M9
M10
M1
M12
M19
M11
M15
M13
M16
M18
M6
M14
M8
M7
M3
-10
0
Avg. log2(Fold Change)
B
LE
MVP
CT
M1
M2
M3
M4
M5
M6
M7
M8
M9
M10
M11
M12
M13
M14
M15
M16
M17
M18
M19
ME Change w.r.t PAN
3
2
1
0
−1
−2
C
Proteins Involved in Glioblastoma
Glycolysis
Proteins Involved in Atherosclerosis
Epithelial Mesenchymal Transition
Apoptosis
TNF−alpha Signaling via NF−kB
Hypoxia
Complement
mTORC1 Signaling
Unfolded Protein Response
Inflammatory Response
KRAS Signaling Up
UV Response Up
Cellular Response to Hypoxia
Cellular Response to Decreased Oxygen
Regulation of Chemokine Production
Positive Regulation of Phagocytosis
Microglial Cell Activation
Synapse Pruning
Positive Regulation of Cytokine Production
Positive Regulation of Endocytosis
Response to Fibroblast Growth Factor
Leptin and CCK8 Activate Nodose Ganglia
M2
M4
M5
M17
log10(Enrich)
1.5
2.0
2.5
3.0
3.5
4.0
−log10(P)
8
6
4
D
Pyrithione
CELECOXIB
DEXAMETHASONE
ARSENIC TRIOXIDE
FLUTICASONE
RITUXIMAB
TACROLIMUS
TRASTUZUMAB
Alitretinoin
Menadione
Gossypol
Methysergide
M4
M5
M17
log10(Enrich)
2.1
2.2
2.3
2.4
2.5
2.6
−log10(P)
3.8
3.6
3.4
E
LR Pair
IL1B_IL1R2
TGFA_EGFR_ERBB2
BDNF_NTRK2
SPP1_CD44
MIF_CD74_CXCR4
SPP1_ITGAV_ITGB1
FN1_CD44
SPP1_ITGA5_ITGB1
JAG1_NOTCH3
JAG1_NOTCH1
CNTN1_NOTCH1
Mast_MES−like
MES−like_Mast
MES−like_MES−like
MES−like_Mono
MES−like_Plasma B
MES−like_RG
Mono_MES−like
Plasma B_MES−like
RG_MES−like
P−Value
Pval adj < 0.05
Pval adj > 0.05
Comm. Score
High
Low
F
T-Val
15
10
5
M4
M2
M17
SPP1_CD44
SPP1_ITGA5_ITGB1
MIF_CD74_CXCR4
SPP1_ITGAV_ITGB1
JAG1_NOTCH3
FN1_CD44
JAG1_NOTCH2
JAG1_NOTCH1
BDNF_NTRK2
CNTN1_NOTCH1
LRRC4C_PTPRF
G
1512-A, IVY Regions
CT
MVP
PAN
LE
FN1_CD44
M2
-10 -5 0 5
MIF_CD74_CXCR4
M4
-5 0 5
H
IER2
FOSB
M17
FOS
JUNB
GADD45B
ZFP36
MCL1
EGR1
DUSP1
SOCS3
M2
SERPINE1
IGFBP2
TIMP1
VEGFA
TNFRSF12A
ANXA2
ADM
VIM
AKAP12
CD151
FLNA
TAGLN2
M4
LOX
ANGPTL4
TUBA1C
NDRG1
CA12
HILPDA
SLC2A1
CD63
FCER1G
M5
LAPTM5
TYROBP
APOC1
C1QB
C1QA
C3
FCGR3A
C1QC
CD74

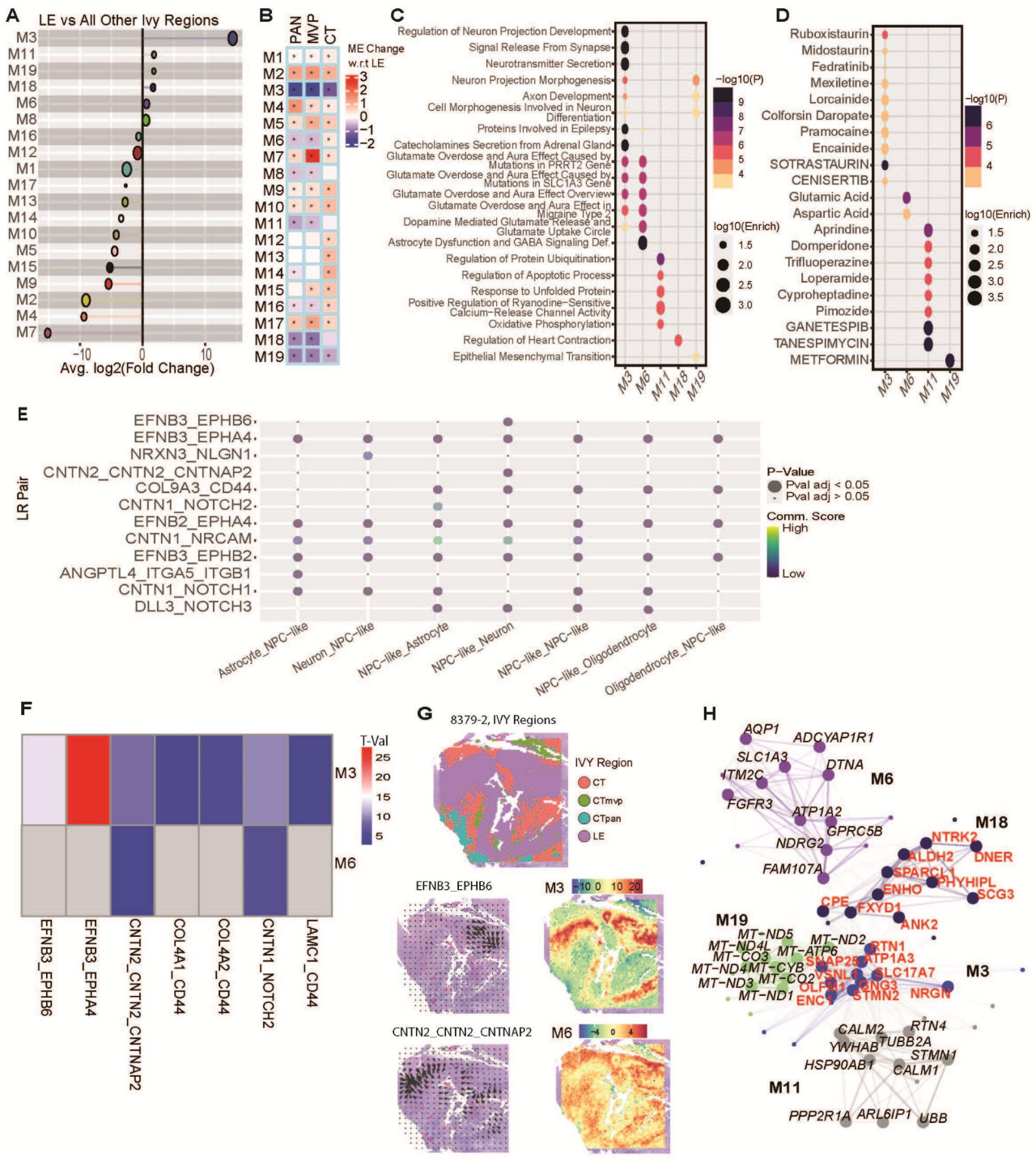
A
LE vs All Other Ivy Regions
M3
M11
M19
M18
M6
M8
M16
M12
M1
M17
M13
M14
M10
M5
M15
M9
M2
M4
M7
−10
0
10
Avg. log2(Fold Change)
B
PAN
MVP
CT
ME Change w.r.t LE
3
2
1
0
−1
−2
M1
M2
M3
M4
M5
M6
M7
M8
M9
M10
M11
M12
M13
M14
M15
M16
M17
M18
M19
C
Regulation of Neuron Projection Development
Signal Release From Synapse
Neurotransmitter Secretion
Neuron Projection Morphogenesis
Axon Development
Cell Morphogenesis Involved in Neuron Differentiation
Proteins Involved in Epilepsy
Catecholamines Secretion from Adrenal Gland
Glutamate Overdose and Aura Effect Caused by Mutations in PRRT2 Gene
Glutamate Overdose and Aura Effect Caused by Mutations in SLC1A3 Gene
Glutamate Overdose and Aura Effect Overview
Glutamate Overdose and Aura Effect in Migraine Type 2
Dopamine Mediated Glutamate Release and Glutamate Uptake Circle
Astrocyte Dysfunction and GABA Signaling Def.
Regulation of Protein Ubiquitination
Regulation of Apoptotic Process
Response to Unfolded Protein
Positive Regulation of Ryanodine−Sensitive Calcium−Release Channel Activity
Oxidative Phosphorylation
Regulation of Heart Contraction
Epithelial Mesenchymal Transition
M3
M6
M11
M18
M19
−log10(P)
9
8
7
6
5
4
log10(Enrich)
1.5
2.0
2.5
3.0
D
Ruboxistaurin
Midostaurin
Fedratinib
Mexiletine
Lorcainide
Colforsin Daropate
Pramocaine
Encainide
SOTRASTAURIN
CENISERTIB
Glutamic Acid
Aspartic Acid
Aprindine
Domperidone
Trifluoperazine
Loperamide
Cyproheptadine
Pimozide
GANETESPIB
TANESPIMYCIN
METFORMIN
M3
M6
M11
M19
−log10(P)
6
5
4
log10(Enrich)
1.5
2.0
2.5
3.0
3.5
E
LR Pair
EFNB3_EPHB6
EFNB3_EPHA4
NRXN3_NLGN1
CNTN2_CNTN2_CNTNAP2
COL9A3_CD44
CNTN1_NOTCH2
EFNB2_EPHA4
CNTN1_NRCAM
EFNB3_EPHB2
ANGPTL4_ITGA5_ITGB1
CNTN1_NOTCH1
DLL3_NOTCH3
Astrocyte_NPC−like
Neuron_NPC−like
NPC−like_Astrocyte
NPC−like_Neuron
NPC−like_NPC−like
NPC−like_Oligodendrocyte
Oligodendrocyte_NPC−like
P−Value
Pval adj < 0.05
Pval adj > 0.05
Comm. Score
High
Low
F
T-Val
25
20
15
10
5
M3
M6
EFNB3_EPHB6
EFNB3_EPHA4
CNTN2_CNTN2_CNTNAP2
COL4A1_CD44
COL4A2_CD44
CNTN1_NOTCH2
LAMC1_CD44
G
8379-2, IVY Regions
IVY Region
CT
CTmvp
CTpan
LE
EFNB3_EPHB6
M3
−10 0 10 20
CNTN2_CNTN2_CNTNAP2
M6
−4 0 4
H
AQP1
ADCYAP1R1
SLC1A3
DTNA
ITM2C
M6
FGFR3
ATP1A2
GPRC5B
NDRG2
M18
NTRK2
ALDH2
DNER
FAM107A
SPARCL1
PHYHIPL
ENHO
SCG3
CPE
FXYD1
ANK2
M19
MT−ND5
MT−ND2
MT−ND4L
MT−ATP6
MT−CO3
RTN1
MT−ND4
MT−CYB
SNAP25
ATP1A3
MT−CO2
VSNL1
SLC17A7
MT−ND3
OLFM1
GNG3
MT−ND1
ENC1
STMN2
NRGN
M3
CALM2
RTN4
YWHAB
TUBB2A
STMN1
HSP90AB1
CALM1
M11
PPP2R1A
ARL6IP1
UBB